

# Nutrient Pumping by Submesoscale Circulations in the Mauritanian Upwelling System

P. J. Hosegood<sup>a</sup>, P. D. Nightingale<sup>b</sup>, A. P. Rees<sup>b</sup>, C. E. Widdicombe<sup>b</sup>, E. M. S. Woodward<sup>b</sup>, D. R. Clark<sup>b</sup>, R. J. Torres<sup>b,1</sup>

<sup>a</sup>*Plymouth University, Drake Circus, Plymouth, PL4 8AA*

<sup>b</sup>*Plymouth Marine Laboratory, Prospect Place, The Hoe, Plymouth, PL1 3DH*

---

## Abstract

Observations made within a cold filament in the Mauritanian upwelling system demonstrate that intense submesoscale circulations at the peripheral edges of the filament are likely responsible for anomalously high levels of observed primary productivity by resupplying nutrients to the euphotic zone. Measurements made on the shelf within the recently upwelled water reveal that primary production (PP) of  $8.2 \text{ gC/m}^{-2} \text{ day}^{-1}$  was supported by nitrate concentrations (NC) of  $8 \text{ mmol m}^{-3}$ . Towards the front that defined the edge of the filament containing the upwelled water as it was transported offshore, PP dropped to  $1.6 \text{ gC m}^{-2} \text{ day}^{-1}$  whilst NC dropped to  $5.5 \text{ mmol m}^{-3}$ . Thus, whilst the observed nutrients on the shelf accounted for 90% of new production, this value dropped to  $\sim 60\%$  near the filament's front after accounting for vertical turbulent fluxes and Ekman pumping. We demonstrate that the  $\text{N}^{15}$  was likely to have been supplied at the front by submesoscale circulations that were directly measured as intense vertical velocities  $\geq 100 \text{ m day}^{-1}$  by a drifting acoustic Doppler current profiler that crossed a submesoscale surface temperature front. At the same time, a recently released tracer was subducted out of the mixed layer within 24 hours of release, providing direct evidence that the frontal circulations were capable of accessing the reservoir of nutrients beneath the pycnocline. The susceptibility of the filament edge to submesoscale instabilities was demonstrated by  $O(1)$  Rossby numbers at horizontal scales of 1-10 km. The frontal circulations are consistent with instabilities arising from a wind-driven nonlinear Ekman buoyancy flux generated by the persistent northerly wind stress that has a down-front

---

<sup>1</sup>Corresponding author

component at the northern edge of the inshore section of the filament. The prevalence of submesoscale instabilities and their associated vertical circulations are proposed to be a key mechanism operating at sub-grid scales and sustaining new production throughout the upwelling system.

*Keywords:* Mauritanian upwelling system, submesoscale circulation, nutrient fluxes, filament, subduction

---

## 1 Introduction

2 Nutrients play a key role in stimulating primary production within the eu-  
3 photic ocean. Where dynamic processes such as eddy pumping (McGillicuddy  
4 et al., 2007) and frontal processes inject nutrients into the euphotic zone, pro-  
5 ductivity is enhanced, whereas in stratified regions where vertical exchange  
6 is limited, biological productivity is low. Understanding the processes that  
7 regulate this vertical exchange is key to understanding not just the initial  
8 stimulus provided to the phytoplankton community by the injection of nu-  
9 trients but also the ongoing production that can be sustained by a persistent  
10 resupply of nutrients from beneath the euphotic zone. Similarly, the organi-  
11 cally bound nutrients are eventually remineralised back into their inorganic  
12 forms at depth following export from the surface layers; the rate at which this  
13 is achieved is directly proportional to the vertical exchanges processes occur-  
14 ring across the base of the surface mixed layer and has global implications  
15 for the export of carbon to the deep ocean.

16 Within eastern boundary currents in the northern hemisphere seasonal or  
17 persistent northerly wind stress drives the coastal upwelling of cold, nutrient  
18 rich water to the surface where it is separated from the warmer offshore water  
19 by a sharp front (Ikeda and Emery, 1984; Capet et al., 2008a; Meunier et al.,  
20 2012). Within the euphotic zone near the surface, the combination of light  
21 availability and high nutrient concentrations inshore of the front promotes  
22 conditions favourable for primary production. Highest production occurs  
23 within the mid-shelf region (Huntsman and Barber, 1977); nearer to the  
24 coast, turbidity reduces light penetration whereas further offshore nutrient  
25 levels decline following uptake by the planktonic community. The globally  
26 important high levels of carbon fixation achieved within such upwelling sys-  
27 tems make it necessary to understand the dynamics that control both the  
28 initial supply of nutrients to the euphotic zone through upwelling, their re-  
29 supply by cross-front exchange, and their distribution throughout the upper

30 ocean in response to vertical mixing processes.

31 The regional dynamical context of upwelling systems is dominated by  
32 the stability and structure of the coastal front separating the nutrient rich  
33 upwelled water from the warmer, stratified offshore water within which nu-  
34 trients are typically depleted and thus primary production limited (Gruber  
35 et al., 2011). Numerous studies have demonstrated that coastal fronts formed  
36 in response to upwelling are subject to baroclinic instabilities that lead to the  
37 formation of mesoscale filaments within which the upwelled water is trans-  
38 ported hundreds of kilometres offshore. The role of topography in destabi-  
39 lizing upwelling fronts remains subject to some debate but has been cited as  
40 a key factor (Narimousa and Maxworthy, 1989) due to the persistent pres-  
41 ence of filaments at topographic features such as promontories and headlands  
42 (Meunier et al., 2012).

43 The mesoscale environment typical of the filaments is characterised by  
44 small Rossby Numbers,  $Ro = \zeta/f$ , where  $\zeta = \frac{\partial v}{\partial x} - \frac{\partial u}{\partial y}$  is the relative vorticity  
45 and  $f$  is the local Coriolis parameter. For small  $Ro$  the flow is geostrophically  
46 balanced and constrained to flow along the front that bounds the filament.  
47 A reduced cross-front exchange inhibits the resupply of nutrients to the fil-  
48 aments and thus new production in the upwelling filament is limited by the  
49 magnitude of the initial injection of nutrients. As the upwelled water is  
50 transported offshore, new production draws down the nutrients, reducing  
51 their concentration and the new production that can be supported by them.  
52 Nutrients can be replaced by vertical fluxes arising from turbulent mixing  
53 across the mixed layer base and Ekman pumping, for example as suggested  
54 for the South China Sea where the two mechanisms combined control regional  
55 growth in the phytoplankton community (Li et al., 2016). As  $Ro$  approaches  
56 unity, however, a different class of dynamics referred to as submesoscales  
57 emerges and leads to the loss of geostrophic control of large scale fronts and  
58 the initiation of cross-frontal exchange by three-dimensional motions.

59 Characterised by length scales of 1-10 km and evolution timescales of  
60  $O(1 \text{ day})$ , submesoscales trigger vertical velocities an order of magnitude  
61 larger than the  $O(10 \text{ m day}^{-1})$  associated with the mesoscale (Mahadevan  
62 and Tandon, 2006). They have been implicated in catalysing the supply of  
63 nutrients to the surface at frontal zones (Levy et al., 2001; Lévy et al., 2012)  
64 and elevating vertical buoyancy fluxes by slumping lateral density fronts  
65 at the periphery of eddies, thereby creating a patchy bloom environment  
66 within the north Atlantic 20-30 days earlier than would occur through heating  
67 alone (Mahadevan et al., 2012). Within eastern boundary current upwelling

68 systems, submesoscales have been demonstrated to be potentially important  
69 at the periphery of filaments where the locally enhanced vertical velocities  
70 may resupply nutrients to the surface layers within the upward branch of the  
71 circulation and permit cross-front exchange in a manner not permitted at low  
72 Rossby numbers (Capet et al., 2008a,b). Similarly, the downward branch of  
73 the submesoscale circulation exports phytoplankton and has been suggested  
74 to dominate over nitrate input within the upward branch in coastal upwelling  
75 systems (Lathuiliere et al., 2010). Observations of this process remain scarce,  
76 however.

77 To address this knowledge gap, we present in this paper results from the  
78 ICON (The Impact of Coastal upwelling on the air-sea exchange of climati-  
79 cally important gases) cruise conducted between April 15 - May 16, 2009 in  
80 the Cap Blanc region (Fig. 1). The aim of the ICON cruise, which was a com-  
81 ponent of the UK contribution to SOLAS (Surface Ocean Lower Atmosphere  
82 Study) was to determine the coastal and shelf influence on microbiological  
83 activity and chemical interactions in an eastern boundary current upwelling  
84 system. Observations of nutrient concentrations and new production within a  
85 mesoscale filament created by upwelling and subsequent eddy-interaction re-  
86 veal a higher level of productivity than can be explained by the initial supply  
87 of nutrients and subsequent draw-down. We show from direct observations  
88 that the regional environment is conducive to the generation of submesoscale  
89 instabilities at the filament periphery due to a loss of geostrophic balance.  
90 The resulting three-dimensional circulations are then potentially responsible  
91 for resupplying additional nutrients to the water within the filament and  
92 maintaining higher levels of new production than can be explained by the  
93 initial nutrient supply at the coast.

94 The paper is structured as follows; we firstly provide the experimental  
95 details, of which many are described in Meunier et al. (2012) such that we  
96 here provide only the additional context necessary to understand the obser-  
97 vations presented in this paper. Particular attention is given to explaining  
98 the estimates of new production and nutrient uptake. We then present the  
99 results in three subsections to demonstrate the mismatch of nutrients and  
100 new production within the filament, the structure of the filament edges that  
101 render them susceptible to submesoscale instabilities, and finally the direct  
102 evidence for energetic vertical circulations associated with the frontal struc-  
103 tures within the region. The implications of our results are then discussed  
104 before conclusions are drawn in the final section.

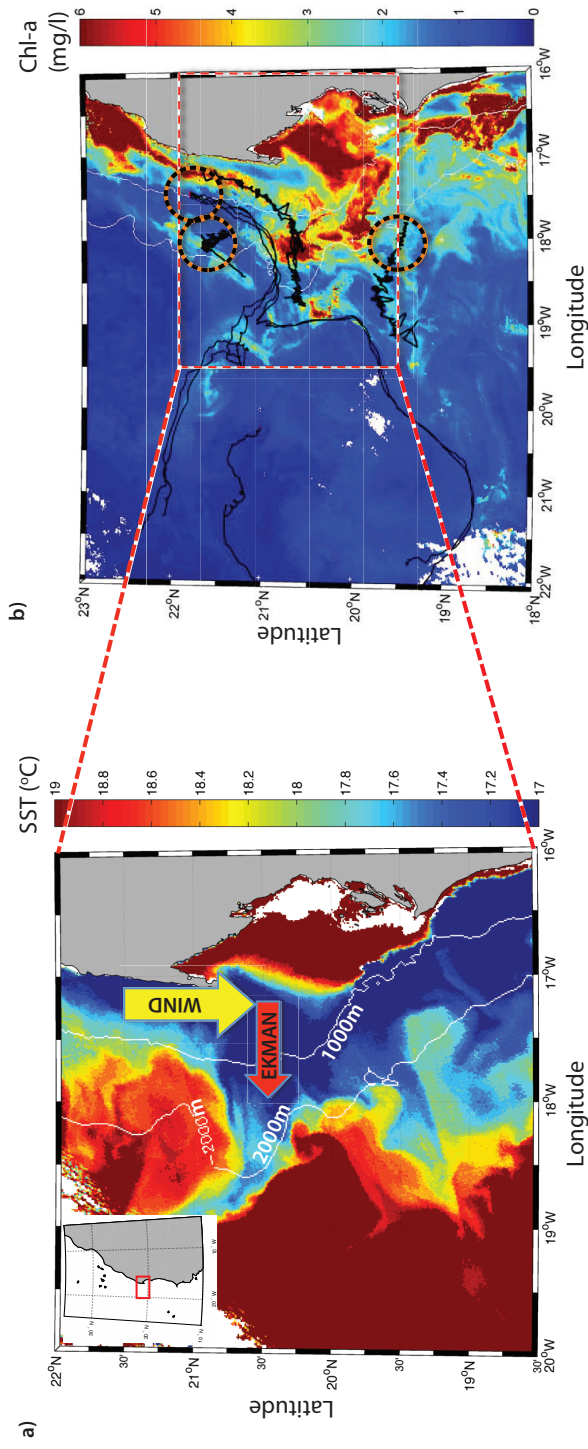


Figure 1: a) Sea surface temperature (SST) and chlorophyll-a throughout the Cap Blanc region on April 27, 2009. The northerly wind stress and resulting offshore Ekman transport generates coastal upwelling inshore of the coastal front apparent in a) as the transition from warm water offshore of the 1000m isobath and the cooler ( $\leq 17.5^{\circ}\text{C}$ ) water adjacent to the coast. The upwelled water is transported offshore within mesoscale filaments, an example of which is evident in a) at a latitude of  $20.5^{\circ}\text{N}$  and represents the primary filament surveyed during the cruise. The frontal environment and high concentrations of nutrients is conducive to high levels of primary production that are strongly correlated with the periphery of the main filaments. Black dashed circles in b) indicate the starting regions within which the drifters used to mark the tracer were released at the beginning of each Lagrangian experiment and the solid black lines their subsequent paths.

## 105 2. Experimental details and methods

### 106 2.1. Oceanographic observations

107 The ICON cruise was conducted aboard the *RRS Discovery* over the pe-  
108 riod  $t = 105 - 131$ , where  $t$  is decimal year day 2009. The study region  
109 encompassed the upwelling system off the coast of Cap Blanc where wind  
110 stress was consistently directed to the south and thus generated an eastward  
111 offshore Ekman transport at the surface. The mechanisms leading to the for-  
112 mation of upwelling filaments has been discussed in a recent paper (Meunier  
113 et al., 2012) but can be summarized as an interaction between the external  
114 eddy field, topographic effects and the upwelled water. The region is situated  
115 within the boundary between salty North Atlantic Central Water (NACW)  
116 and the fresher South Atlantic Central Water (SACW). A zonal front forms  
117 between the water masses across the tropical north Atlantic but reorientates  
118 itself to a south-west/north-east heading near the African coast where it is  
119 referred to as the Cap Verde Frontal Zone (CVFZ). Despite a relatively weak  
120 density signature associated with the largely compensated front, baroclinic  
121 along-front jets inhibit cross-frontal exchange although the interleaving of  
122 water masses has been observed to facilitate the large-scale cross-front ex-  
123 change of properties (Perez-Rodriguez et al., 2001; Martínez-Marrero et al.,  
124 2008).

125 Two different sampling strategies were employed throughout the cruise  
126 and are illustrated in Fig. 2. To map the three-dimensional structure and  
127 physical properties of the filaments, ship-based towed conductivity-temperature-  
128 depth (CTD) and vessel-mounted acoustic Doppler current profiler (ADCP)  
129 surveys were undertaken. To monitor the temporal evolution of recently up-  
130 welled water, Lagrangian measurements were made of a parcel of water after  
131 releasing an inert tracer. Each approach is outlined below.

#### 132 2.1.1. Ship-based surveys

133 Ship-based quasi-synoptic filament surveys consisted of multiple transects  
134 that were orientated perpendicular to the principal axis of the filament and  
135 aimed to cross the fronts on each side. Standard CTD parameters were  
136 measured using the Moving Vessel Profiler (MVP). The MVP consists of a  
137 fish that houses an Applied Microsystems Laboratory (AML) micro-CTD  
138 sampling at 25 Hz, AML micro-dissolved oxygen and Atlantic irradiance  
139 sensors, and Chelsea Instruments MiniTracka fluorometer. The fish free-falls  
140 at a vertical rate of  $1 \text{ m s}^{-1}$  to a depth of 350 m before being recovered to

141 the surface whilst the ship is underway. At a speed of 8 knots, a complete  
142 profiling cycle that includes both the downward and upward profiles (the  
143 former is vertical but the latter profile is oblique and near horizontal during  
144 recovery throughout the upper 50 m) was completed during a horizontal  
145 distance of  $\leq 2$  km. Data are subsequently gridded to 1 km horizontal and  
146 1 m vertical resolution using the Barnes algorithm (Barnes, 1994). Velocity  
147 measurements were acquired using the hull-mounted 150kHz RDI ADCP as  
148 8 m vertical bins to a depth of typically 320 m and averaged to 10 minute  
149 ensembles.

### 150 *2.1.2. Lagrangian observations*

151 A Lagrangian reference frame was employed to monitor the temporal evo-  
152 lution of the near-surface biogeochemical regime and its response to the in-  
153 jection of nutrients following upwelling. At the beginning of each Lagrangian  
154 experiment, of which there were three during the cruise and are henceforth  
155 referred to as Patches 1-3, a quantity of SF<sub>6</sub> tracer was released within the  
156 surface mixed layer around a drogued drifter. The purpose of the SF<sub>6</sub>, which  
157 is an inert tracer, was to enable the verification of the patch location, prop-  
158 erties and evolution by monitoring its concentration at a depth of 5 m where  
159 the ship's intake was located and during vertical casts. The tracer deploy-  
160 ment and SF<sub>6</sub> analysis followed those used in Nightingale et al. (2000). The  
161 origin of each patch was defined by the position of the central drogued drifter  
162 equipped with a radio transmitter that reported its location back to the ship  
163 at 5 minute intervals. Four further drifters were positioned at each of the  
164 corners of the initial SF<sub>6</sub> release so that the whole patch could be constantly  
165 monitored from the ship. The centre of the patch was estimated following  
166 the nighttime sampling as the centre of mass of the SF<sub>6</sub> (Loucaides et al.,  
167 2012). The centre of the patch was then the location where vertical mi-  
168 crostructure profiles and water samples were obtained at regular intervals  
169 during the following daytime.

170 Immediately following each release of the tracer, two drogued and instru-  
171 mented drifters were deployed. Each drifter was equipped with a surface  
172 satellite tracked beacon and a drogue of 6 m length between a depth of 9-14  
173 m following standard WOCE specification. The primary drifter was equipped  
174 with a Wirewalker (Pinkel et al., 2010) on which was mounted a RBR CTD.  
175 The Wirewalker repeatedly ascends to the surface under its own buoyancy  
176 before being pulled back to its starting depth of 70 m by a ratchet mechanism  
177 driven by surface wave action. Vertical CTD profiles were thereby obtained

178 every 10 minutes approximately during the ascent of the Wirewalker whilst  
 179 the drifter was advected horizontally by the mean flow at 15 m depth. The  
 180 CTD sampled at 6 Hz; at an ascent rate of approximately  $0.2 \text{ m s}^{-1}$ , raw  
 181 data were obtained with a vertical resolution of 0.03 m.

182 The second drifter was equipped with a downward looking 600 kHz RDI  
 183 Broadband ADCP located at 20 m depth, immediately beneath the drogue  
 184 and isolated from surface motion by using a rubber chord of 3 inch diameter to  
 185 attach the surface buoyancy to the drogue. A  $1.5 \text{ m}^2$  square plate mounted on  
 186 the top of the submersible ensured the horizontal orientation of the platform.  
 187 The ADCP was set to sample in Mode 12 with 3 pings per 3 second ensemble  
 188 in 0.5 m vertical bins. Maximum range was 44 m from the instrument such  
 189 that with a 2.2 m blanking distance, velocity measurements were obtained  
 190 between 24-68 m. The vertical velocities were adjusted for the ADCP vertical  
 191 movement prior to averaging the data into 10 minute ensembles.

192 CTD water samples and microstructure profiles were acquired during day-  
 193 time throughout each Lagrangian experiment. The microstructure profiles  
 194 acquired with the ISW Microstructure Sensor System (MSS) provide esti-  
 195 mates of the dissipation rate of turbulent kinetic energy,  $\epsilon = 7.5\mu\langle(\frac{\partial u}{\partial z})\rangle$ ,  
 196 where the angle brackets denote spatial averaging over typically 1 m and  $u$   
 197 represents the turbulent velocity component. The kinematic viscosity of wa-  
 198 ter  $\mu$  is approximated from the measured temperature using the polynomial:

$$\mu = 1.792747 - 0.05126103 \times T \times 0.0005918645T^2 \quad (1)$$

199 The vertical eddy diffusivity was then computed following Osborn (1980)  
 200 as  $K_z = \Gamma \frac{\epsilon}{N^2}$  where  $\Gamma=0.2$  is the mixing efficiency and  $N = \sqrt{-\frac{g}{\rho_o} \frac{\partial \rho}{\partial z}}$  is the  
 201 Brunt-Vaisala frequency. Vertical turbulent nutrient fluxes were then esti-  
 202 mated as  $F_{nut} = K_z \frac{\partial(Nut)}{\partial z}$  where  $Nut$  is the observed nutrient concentration  
 203 from the CTD water samples and  $K_z$  is estimated as the mean value across  
 204 the base of the mixed layer.

205 Within this paper we focus on a subset of observations to demonstrate  
 206 the potential role played by submesoscales in supplying nutrients at the pe-  
 207 ripheral edges of filaments. We use primarily the results from Patches 1 and  
 208 2, corresponding to the periods  $t=113-120$  and  $t=128-130$ , respectively, and  
 209 from the survey of the primary filament between  $t=120-125$  within which  
 210 Patch 1 was carried out. Within the Discussion we briefly refer to patch 3  
 211 for which Lagrangian measurements were made but for which no ship-based  
 212 filament survey was possible due to the malfunction of the MVP.



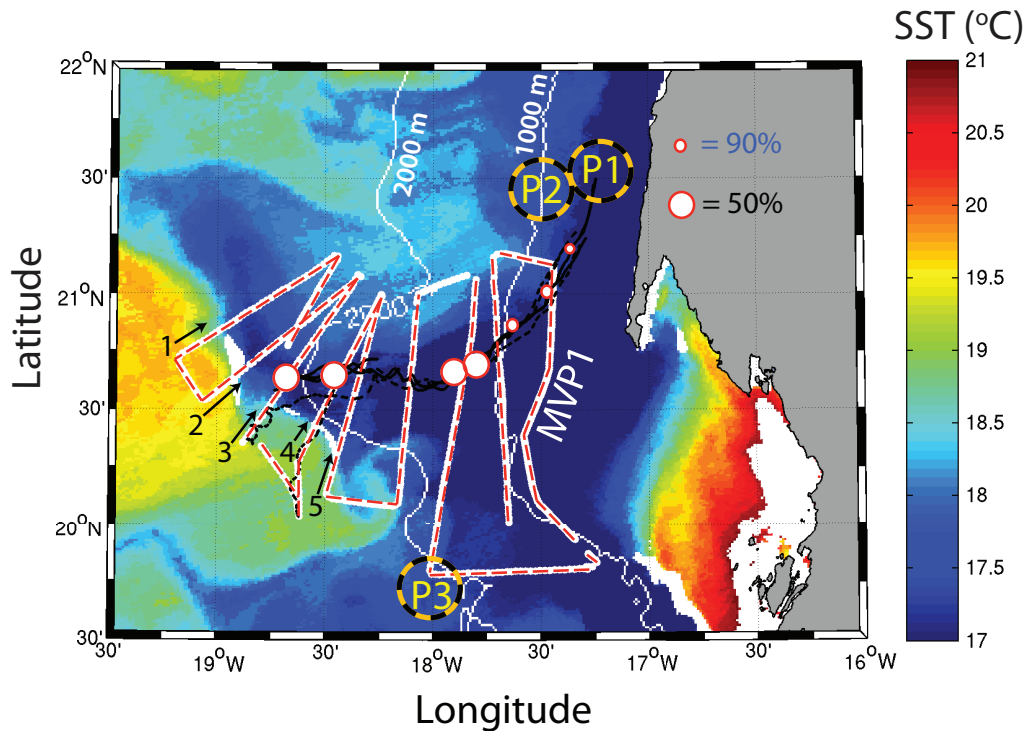


Figure 2: Sea surface temperature (SST) within the study region. Overlain (white/red-dashed lines) is the ship-track for the MVP/VM-ADCP survey of the primary filament (MVP1) within which Patch 1 was conducted. Legs 1-5 for which detailed results are presented in Fig. 6 are labelled accordingly. The initial location of each patch experiment (labelled P1, P2 and P3, respectively) where the SF<sub>6</sub> was released are indicated by the orange/black dashed circles. Note that the time that passed between P1 and P3 exceeded 3 weeks and thus the SST field, which corresponds to April 27 and thus towards the end of P1, evolved significantly by the time that P3 was initiated. The white circles (red outlines) along the ship track during MVP1 indicate the magnitude of the mismatch between the predicted new production based on available nutrients and the observed new production.

213 *2.2. Remote sensing*

214 Sea surface temperature (SST) data were provided by the NERC Earth  
215 Observation Data Acquisition and Analysis Service (NEODAAS) through-  
216 out the cruise to enable the identification of the surface temperature fronts  
217 that marked the edge of the filaments. Coverage throughout the cruise was  
218 generally unimpeded by cloud cover. Data are derived from AVHRR with 1  
219 km resolution; full details of processing are available at <http://rsg.pml.ac.uk>.  
220 Sea surface chlorophyll was also provided by NEODAAS derived from ocean  
221 colour data obtained through the Aqua sensor in the MODIS satellite.

222 Surface winds were obtained from Remote Sensing Systems Cross-Calibrated  
223 Multi-Platform (CCMP) product at a horizontal resolution of  $0.25^\circ$ .

224 *2.3. Biological measurements: new production estimates*

225 In order to make estimates of the new production, routine measurements  
226 of nutrients, primary production, f-ratios and plankton community were un-  
227 dertaken during both patch 1 and patch 3 from discrete water samples. The  
228 water samples were collected before dawn using Niskin bottles mounted on  
229 the CTD rosette frame at generally eight depths from which at least six  
230 included the euphotic layer and one was at the top five meters. Nutrient  
231 measurements of silicate, phosphate, nitrate, nitrite and ammonia were  
232 measured colorimetrically using a Bran and Luebbe AAIH segmented flow  
233 autoanalyzer (Woodward and Rees, 2001). Primary production was esti-  
234 mated from six light depths (1, 7, 20, 33, 55 and 97% of incident light) and  
235 distributed into triplicate 60ml polycarbonate bottles and inoculated with  
236  $\sim 10 \mu\text{Ci } ^{14}\text{C-bicarbonate}$ . Incubations were performed in on-deck incuba-  
237 tors under simulated in-situ light conditions and temperature controlled by  
238 surface seawater. Experiments were terminated after 24 hours by sequential  
239 filtration through 2 and  $0.2\mu\text{m}$  Supor 200 membrane filters for particulate  
240 organic production. Samples were fumed with HCl prior to onboard liq-  
241 uid scintillation counting. Water samples from the same depths were used  
242 for quantifying the phytoplankton and microzooplankton community com-  
243 position and abundance from microscopic analysis of samples preserved with  
244 Lugol's iodine. Cells were identified to species-level where possible in accor-  
245 dance with Tomas 2006 and assigned to three functional groups (Diatoms  
246 (centric and pennate), Dinoflagellates and Flagellates). The conversion from  
247 cell numbers to biomass was based on volumes according to geometric shapes  
248 and formulae of Olenina et al. (2006) and of Menden-Deuer and Lessard  
249 (2000).

250 Even under upwelling conditions, nitrification, the sequential oxidation  
 251 of  $\text{NH}_4^+$  through  $\text{NO}_2^-$  to  $\text{NO}_3^-$ , can make a significant contribution to  $\text{NO}_3^-$ ,  
 252 assimilation in the surface ocean (Clark et al., 2011). This complicates the  
 253 new production paradigm, where:

$$\text{Newproduction} = f - \text{ratio} \times \text{Primary Production} \quad (2)$$

254 because  $\text{NO}_3^-$  regenerated within the photic zone cannot be equated to new  
 255 nitrogen. Therefore, f-ratio determinations do not equate to new production  
 256 (Yool et al., 2007) unless simultaneous measurements are made of nitrifica-  
 257 tion and N-assimilation ( $\rho\text{N}$ ). Such measurements are rarely done (Fernández  
 258 I. and Raimbault, 2007; Fernández et al., 2009), but have demonstrated that  
 259 nitrification can provide between 2% and 100% of phytoplankton  $\text{NO}_3^-$  de-  
 260 mand. In this study, we address this aspect by simultaneously assessing  
 261 N-assimilation and nitrification processes, and have adjusted f-ratio determi-  
 262 nation to correct estimates of new production for  $\text{NO}_3^-$  derived from nitrifi-  
 263 cation:

$$F_{nit} - \text{ratio} = \frac{[\rho\text{NO}_3^- \times (1 - \text{regNO}_3^-)]}{(\rho\text{NO}_3^- + \rho\text{NH}_3^-)} \quad (3)$$

264 A brief description of methods is provided here; the reader is referred  
 265 to Clark et al. (2006, 2007, 2011, 2016) for comprehensive details. Nitrogen  
 266 assimilation and nitrification experiments were undertaken on near surface  
 267 waters (5m) to allow estimations of in-situ  $f_{nit}$ -ratios and new production esti-  
 268 mates. For determination of N-assimilation, seawater samples were collected  
 269 into triplicate clear polycarbonate bottles and amended with either  $\text{N}^{15}\text{-NO}_3^-$   
 270 or  $\text{N}^{15}\text{-NH}_4^+$  at approximately 10% of ambient concentrations according to  
 271 Clark et al. (2011). Bottles were transferred to the on-deck incubators for 3  
 272 hours, after which they were filtered onto 25mm GF/F filters. Filters were  
 273 stored frozen until return to the shore based laboratory where they were dried  
 274 at 50°C for 12 hours.  $\text{N}^{15}$  atom and particulate nitrogen concentration were  
 275 determined using continuous flow stable isotope mass spectrometry (Owens  
 276 and Rees, 1989) and rates of uptake corrected for isotope dilution (Clark  
 277 et al., 2011). Rates of nitrification were determined using isotope dilution  
 278 methods. 5 L of unfiltered seawater collected pre-dawn was amended with  
 279  $\text{N}^{15}\text{O}_2^-$  ( $\text{NH}_4^+$  oxidation studies) or  $\text{N}^{15}\text{-NO}_3^-$  ( $\text{NO}_2^-$  oxidation studies).

280 Following the addition of  $\text{N}^{15}$ , samples were mixed and triplicate 500 ml  
 281 samples were removed from each 5 L volume for the determination of pre-  
 282 incubation N concentration and isotopic enrichment. 2.4L of the remaining

283 N<sup>15</sup> enriched seawater was incubated on deck for an average of 9 hours during  
 284 day light. At the end of the incubation period, samples were filtered through  
 285 GF/F filters and triplicate 500 ml volumes were used for the determination  
 286 of post-incubation N concentration and N<sup>15</sup> enrichment. Nitrification sam-  
 287 ples were collected by solid phase extraction, stored frozen and processed  
 288 in the land based laboratory. Samples were eluted from SPE columns and  
 289 deuterated internal standards were added for sample quantification. Sam-  
 290 ples were purified by HPLC and analysed by GCMS. N-regeneration rates  
 291 were derived from end-points using the Blackburn-Caperon model Blackburn  
 292 (1979); Caperon et al. (1979).

#### 293 *2.4. New production budget*

294 After nutrients are upwelled to the euphotic zone on the shelf, water is  
 295 advected offshore within the mesoscale filaments depicted in Fig. 1. Nutrients  
 296 are drawn down by new production, depleting the available nutrients unless  
 297 additional nutrients are supplied laterally from outside the filament or from  
 298 the substantial reservoir beneath the thermocline.

299 All nutrient data were subsequently averaged for the euphotic layer to  
 300 calculate a NO<sub>3</sub><sup>-</sup> based budget during the Lagrangian experiments. The eu-  
 301 photic layer increased from 35 m at the start of patch 1 to 60 m on the last  
 302 day. The euphotic layer was in all occasions shallower than the mixed layer.  
 303 A NO<sub>3</sub><sup>-</sup> budget for the euphotic layer was calculated as  $\Delta\text{Ambient NO}_3^- =$   
 304  $\text{NO}_3^- \text{Uptake} + \text{VerticalNO}_3^- \text{Fluxes}$ . Horizontal contributions are ignored on  
 305 the basis that nutrient concentrations were lower outside the filament and  
 306 would therefore act to remove rather than supply nutrients to the filament  
 307 in which the Lagrangian experiment was performed. From the estimates of  
 308 NO<sub>3</sub><sup>-</sup> Uptake and the observed C:N stoichiometry calculated as Total POC /  
 309 Total PON we estimate the theoretical new production that could have been  
 310 supported by the observed drop in ambient nitrate concentrations compen-  
 311 sated by the observed vertical nitrate fluxes into the euphotic layer.

312 Vertical NO<sub>3</sub><sup>-</sup> fluxes were estimated as the sum of the vertical turbu-  
 313 lent diffusive flux (described above), and the vertical transport from Ekman  
 314 pumping. The Ekman pumping velocity was estimated from the wind stress  
 315 curl (RSS CCMP v2.0, Remote Sensing Systems, www.rmss.com) as

$$w_e = \frac{1}{\rho_w} (\Delta \times \frac{\tau}{f}) \quad (4)$$

316 where  $\rho_w$  is the density of seawater,  $f$  is the coriolis frequency and  $\tau$  is  
317 the wind stress vector. The total nutrient flux to the euphotic zone arising  
318 from turbulent fluxes and Ekman pumping is given by

$$VerticalNO_3^- Fluxes = K_z \frac{\partial C}{\partial z} + w_e C \quad (5)$$

### 319 **3. Results**

320 We demonstrate here that the new production occurring offshore within a  
321 mesoscale filament required additional nutrients than were supplied by initial  
322 upwelling near the coast. We present results in three subsections to highlight  
323 1) the discrepancy between new production and nutrient supply within the  
324 largest filament that was the focus of the first tracer release experiment  
325 (Patch 1) and that 2) the edges of the filament within which Patch 1 was  
326 conducted were susceptible to submesoscale instabilities due to the formation  
327 of regions with high local Rossby number. Direct evidence of the intense  
328 vertical circulations arising due to the emergence of submesoscales is provided  
329 by 3) direct evidence from Patch 2 for the rapid subduction of SF<sub>6</sub> by intense  
330 vertical motions at a submesoscale front, and the direct measurement of the  
331 intense vertical velocities by a drifting ADCP as it crossed a submesoscale  
332 front for which evidence is obtained from a co-located drifting Wirewalker  
333 equipped with a profiling CTD.

#### 334 *3.1. Patch 1: Nutrient concentrations and new production estimates in an* 335 *upwelling filament*

336 Patch 1 began at  $t=112.1$  with the injection of SF<sub>6</sub> into the surface mixed  
337 layer and the release of the drogued drifters. The drifters, and thus the water  
338 parcel that was sampled throughout the following 7 days with CTD, water  
339 samples and microstructure profiling, were located within the upwelled water  
340 approximately 30 km inshore of the front when defined by the position of the  
341 18.15°C isotherm estimated from the AVHRR data (Fig. 4a).

342 During the two days prior to the release of the tracer, a transect was com-  
343 pleted perpendicular to the coast during which surface nitrate concentrations  
344 were measured in addition to a vertical profile to establish the horizontal and  
345 vertical nutrient distributions. The transect began offshore within the fila-  
346 ment, traversed the stratified water that had become entrained around the  
347 meandering front, and finished within the coastal upwelled water (Fig. 3b).

348 Nitrate concentrations were lowest ( $\leq 2 \text{ mmol m}^{-3}$ ) within the stratified wa-  
349 ter, just offshore of the coastal front. Concentrations increased to  $\approx 3 \text{ mmol}$   
350  $\text{m}^{-3}$  further offshore at the stations located within the upwelled water that  
351 had been advected offshore within the filament. Maximum concentrations  
352 were unsurprisingly observed where upwelling occurred, with surface concen-  
353 trations of  $\geq 7 \text{ mmol m}^{-3}$  measured. The subsurface reservoir of nutrients  
354 was clearly evident in the vertical profile that indicated concentrations ap-  
355 proaching  $17 \text{ mmol m}^{-3}$  below 40 m depth (Fig. 3a).

356 Throughout the week following the tracer release the drifter, and thus  
357 upwelled water, was advected offshore within the filament. However, whilst  
358 the track of the drifter largely followed the principal axis of the filament and  
359 described an anticyclonic trajectory, it's distance to the front when defined  
360 by the  $18.15^\circ\text{C}$  isotherm marking the outer edge of the filament decreased  
361 (Fig. 4). Beginning Patch 1 at a distance of 30 km from the front, the primary  
362 drifter encroached to within 10 km of the northern filament edge as the front  
363 turned towards the west. As the filament narrowed offshore and turned back  
364 towards a meridional orientation, the distance between the drifter and front  
365 decreased further until the water samples were essentially being collected  
366 from the frontal region.

367 The Dissolved Inorganic Nitrogen (DIN) pool in surface waters was domi-  
368 nated by  $\text{NO}_3^-$  (86%; 94%), with  $\text{NH}_4^+$  (10%; 2%) and  $\text{NO}_2^-$  (4%; 4%) making  
369 only minor contributions. Concentrations of nitrate in newly upwelled sur-  
370 face waters (day 111) were  $\approx 9.2 \text{ mmol m}^{-3}$  and these reduced progressively  
371 as the filament advected offshore to  $\approx 5.3 \text{ mmol m}^{-3}$  at the end of the exper-  
372 imental period (day 119). The reduction in  $\text{NO}_3^-$  concentrations was largely  
373 associated with high rates of primary production which also decreased with  
374 time from a maximum of  $8.2 \text{ gC m}^{-2}\text{d}^{-1}$  to  $1.2 \text{ gC m}^{-2}\text{d}^{-1}$  and were associ-  
375 ated with surface chlorophyll concentrations which fell from  $\approx 5.5$  to  $0.9 \mu\text{g}$   
376  $\text{m}^{-3}$ .

377 N-assimilation and nitrification were measured simultaneously in the sur-  
378 face waters. High ambient  $\text{NO}_3^-$  concentrations ensured that nitrification  
379 and assimilation were not directly coupled and turnover was relatively low,  
380 in contrast to  $\text{NH}_4^+$  which cycled rapidly. Estimates of  $F_{nit}$ -ratio reflected  
381 proportionally higher  $\text{NO}_3^-$  uptake in newly upwelled waters than in older  
382 waters as the values decrease from 0.62 on day 111 to 0.35 on day 119.

383 The time at which the distance of the drifters from the front decreased  
384 coincided with the time at which the mismatch increased between predicted  
385 new production based on the initial supply of nutrients from the coastal up-

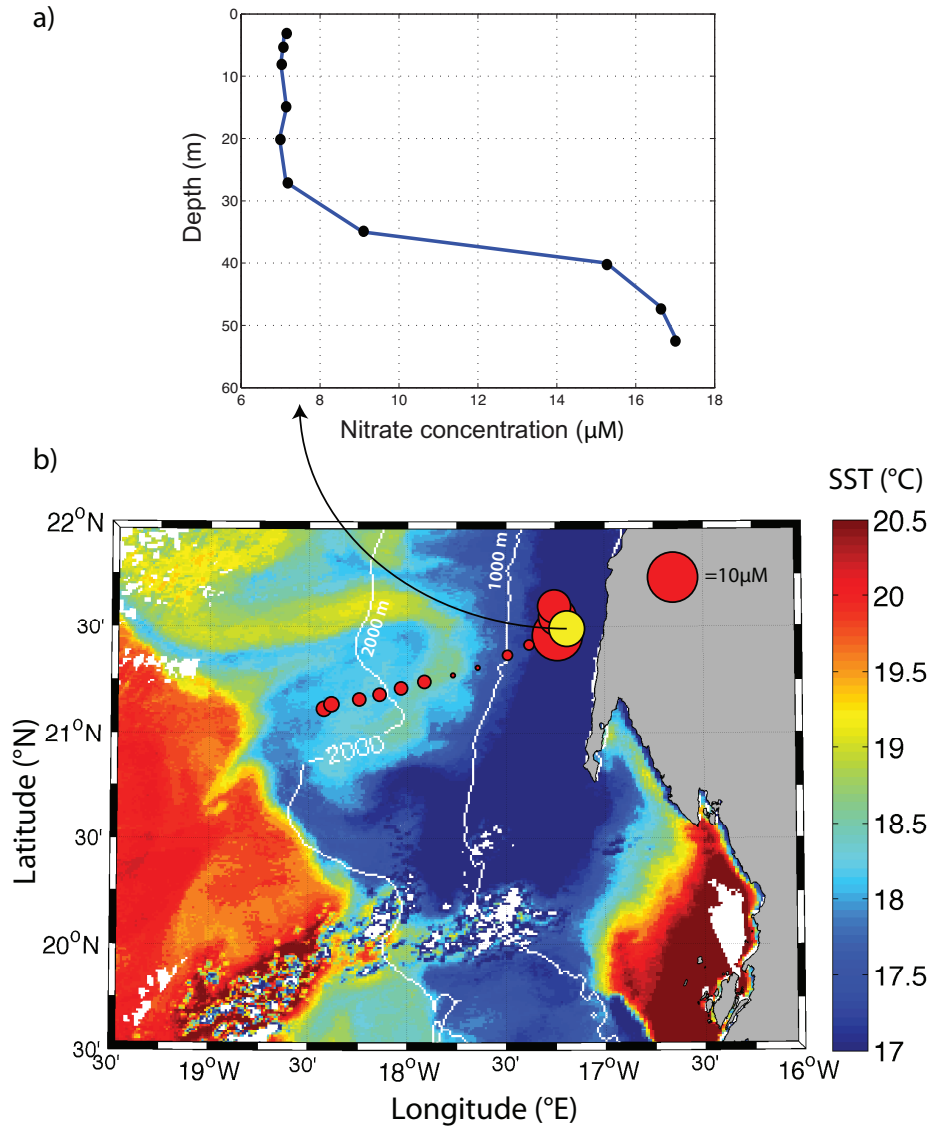


Figure 3: a) Vertical profile of nitrate concentration at the location indicated by the yellow circle in a), indicating the SST ( $^{\circ}\text{C}$ ) throughout study region during day 109 and the surface nitrate concentration (3 m depth) represented by the red circles. The size of the red circles indicate the nitrate concentration. The satellite passed overhead during the night-time of day 109 (20th April, 2009) at the time when the stations furthest inshore were sampled.

386 welling and the observed new production. Immediately following upwelling  
387 at the coast, nitrate concentrations of  $8 \text{ mmol m}^{-3}$  supported equivalently  
388 high primary production of  $8.2 \text{ gCm}^{-2} \text{ day}^{-1}$ . Throughout the seven days  
389 for which the patch was tracked, however, the percentage of primary produc-  
390 tion that was attributable to the observed nitrate decline and vertical fluxes  
391 (computed from the daytime MSS profiles) reduced from 80-90% near the  
392 coast and on the shelf to  $\sim 60\%$  four days later as the drifters moved towards  
393 the northern edge of the filament.

394 The stations on the shelf (corresponding to the first four days of Patch  
395 1) exhibited daily ambient  $\text{NO}_3^-$  decreases between  $0.7\text{-}1.6 \text{ mmol m}^{-3}$  and  
396 daily vertical  $\text{NO}_3^-$  fluxes ranging from  $0.05$  to  $0.1 \text{ mmol m}^{-3} \text{ day}^{-1}$  both  
397 terms balancing the New production mediated  $\text{NO}_3^-$  decline ( $1.2\text{-}2 \text{ mmol m}^{-3}$   
398  $\text{day}^{-1}$ ). On subsequent days when the drifters were closer to the filament  
399 edge, daily ambient  $\text{NO}_3^-$  decreases and vertical fluxes totalling  $0.1\text{-}0.3 \text{ mmol}$   
400  $\text{m}^{-3}$  were not sufficient to explain the New production requirements of  $0.3\text{-}$   
401  $0.7 \text{ mmol m}^{-3} \text{ day}^{-1} \text{ NO}_3^-$ . In both environments (on shelf and inside the  
402 filament), the turbulent vertical fluxes of  $\text{NO}_3^-$  were of similar magnitude  
403 and corresponded to  $\approx 10\%$  of the New production requirements. On the  
404 shelf, the vertical fluxes were characterised by smaller  $K_z$  but larger vertical  
405 nitrate gradients than inside the filament (Fig. 4c,f).

406 Nutrient supply by Ekman pumping was negligible; the region within  
407 which the filament was located was subjected to very weak downwelling ve-  
408 locities of  $\leq 1 \text{ m day}^{-1}$  based on observed winds during day 116. The pre-  
409 vailing wind field changed little in terms of direction or magnitude during  
410 the cruise as is normal for this region. Corresponding nutrient fluxes were  
411 estimated across the region based on a nitrate concentration of  $10 \text{ mmol m}^{-3}$   
412 were thus  $< 2 \mu\text{mol m}^{-2} \text{ day}^{-1}$  (fig. 5). As nitrate concentrations offshore  
413 within the filament were  $< 10 \text{ mmol m}^{-3}$  (Fig. 2e) the estimated fluxes are an  
414 overestimate for the region within which the initial upwelling occurred. We  
415 further note that surface nutrient concentrations outside the filament were  
416 significantly lower than within it, precluding lateral advection of nutrients as  
417 the supply mechanism (fig. 3).

### 418 3.2. Filament survey: Background context

419 Following recovery of the drifters at the end of the Patch 1 Lagrangian  
420 experiment, the principal filament was surveyed with the MVP and the ship-  
421 mounted VM-ADCP. Throughout the 4 days that were required to complete  
422 the survey the filament structure evolved and the results cannot strictly be



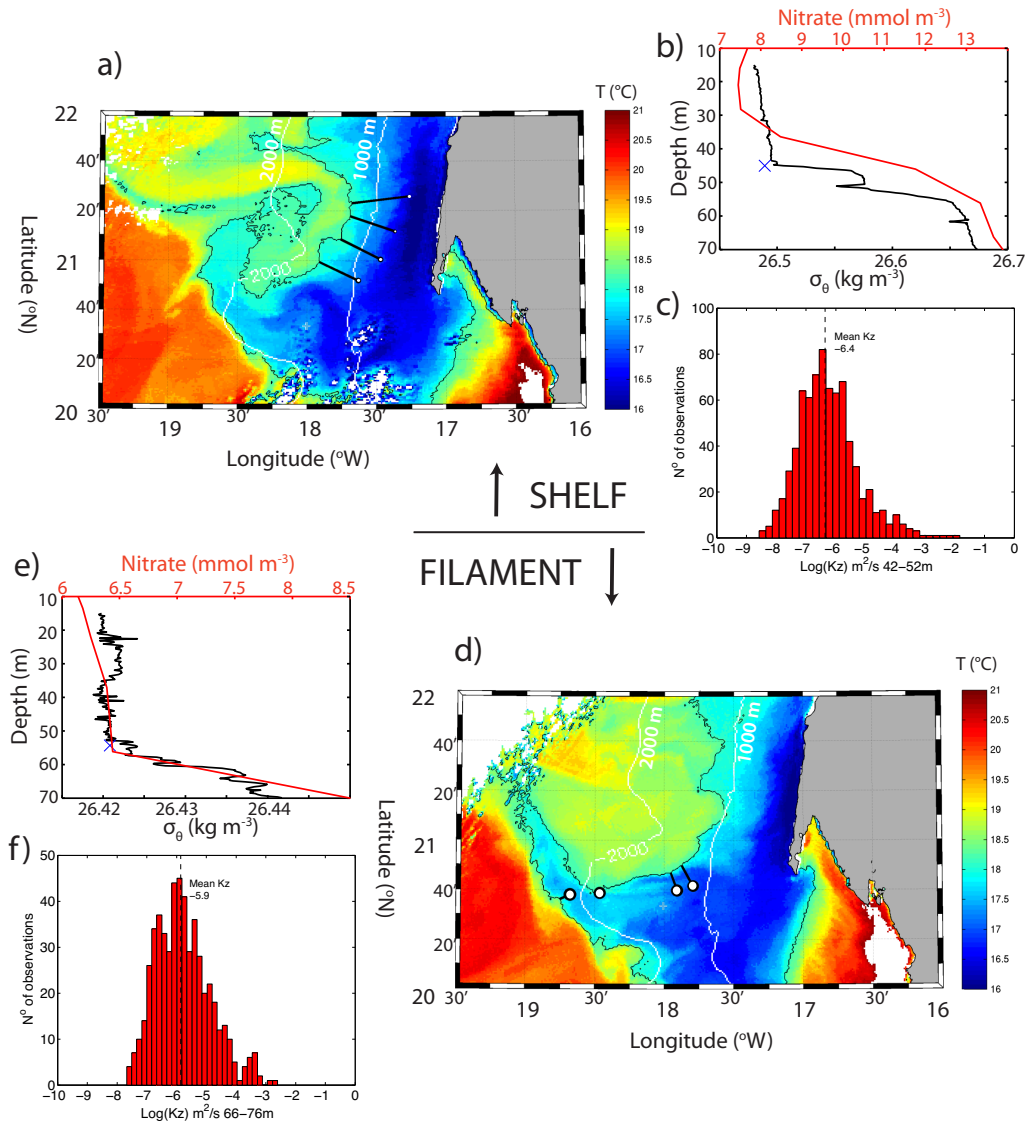


Figure 4: a) SST ( $^{\circ}\text{C}$ ) throughout study region during day 112 and the position of the drogued drifter (black/white dots) over the shelf relative to the nearest location of front at the filament periphery (black line, defined as  $18.15^{\circ}\text{C}$  isotherm), vertical profiles of b) nitrate concentration (red line), and  $\sigma_{\theta}$  (black line) and c) histogram of diapycnal diffusivity,  $K_z$ , across the pycnocline in the shelf region, and d) SST during day 116 when the drifter was entrained into the filament. The corresponding vertical profiles of nitrate and  $\sigma_{\theta}$  are shown in e) and f) the diapycnal diffusivity across the pycnocline, now at 66-76m and thus more than 20m deeper than on the shelf. The depths corresponding to the upper limit of the pycnocline are indicated by the blue crosses in b) and e).

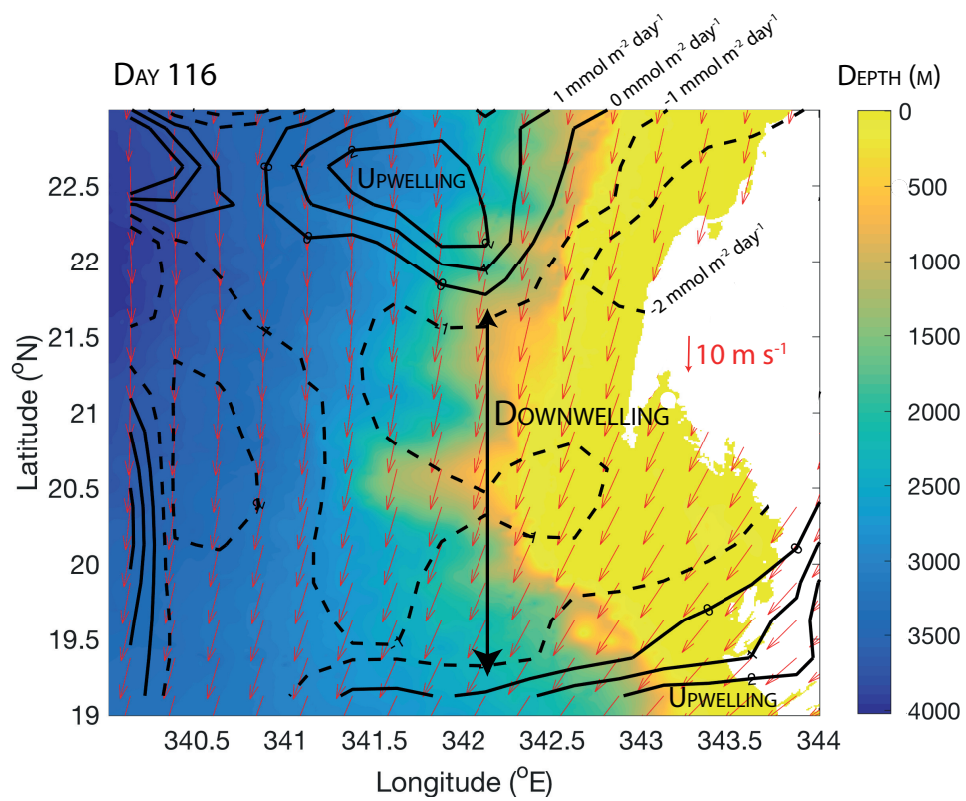


Figure 5: Nitrate flux due to Ekman pumping (contours) driven by the surface winds (red arrows) and assuming a spatially uniform nitrate concentration of  $10 \text{ mmol m}^{-3}$ . Downwelling is indicated by black dashed contours and upwelling by solid black lines. Depth is indicated by the color shading.

423 viewed as synoptic. In particular, SST data indicate that the northern fil-  
424 ament front in Fig. 6 migrated north and weakened throughout MVP1. In  
425 contrast, the front on the southern edge of the filament was typically more  
426 clearly defined and characterised by a stronger temperature gradient due to  
427 the greater influence of the warm SACW in the south.

428 The narrow horizontal extent of the filament at its furthest offshore posi-  
429 tion is revealed by the cooler, fresher water relative to that found at the ends  
430 of each cross-filament transect. The filament core is defined by water at the  
431 surface with temperature  $\leq 19^\circ\text{C}$  and salinity  $\leq 36.0$ . The lateral extent of the  
432 surface signature of the filament varies between each transect but is notably  
433 narrower where the filament approaches the limit of its offshore excursion to  
434 the west. Warmer, more saline water is found to the south of the filament  
435 due to the greater proportion of SACW.

436 The thermohaline gradients associated with the filament were density  
437 compensated to a large extent. Despite clear lateral gradients in both tem-  
438 perature and salinity, isopycnals remained largely horizontal across the fil-  
439 ament. However, within localized regions at the filament edges isopycnals  
440 tend towards the vertical and, at the southern edge furthest offshore, out-  
441 crop. Lateral density gradients exceeding  $0.1 \text{ kg m}^{-3}$  were observed adjacent  
442 to the warmest temperatures, corresponding to a buoyancy gradient,  $b_x$ , of  $1$   
443  $\times 10^{-6} \text{ s}^{-1}$ . The near surface stratification results in small internal Rossby  
444 radii throughout the surface mixed layer (SML),  $Ro_{SML} = NH/f$  where  $N$   
445 is the stratification of the SML defined by the region of depth  $H$  between the  
446 surface and the depth at which density increases by  $0.1 \text{ kg m}^{-3}$  relative to the  
447 surface.  $Ro_{SML}$  is proposed to be the limiting length scale for submesoscale  
448 instabilities (Thomas et al., 2008), and here attained values of  $Ro_{SML} = 2.8$   
449 - 3.9 km. The largest values were found to the north where the near surface  
450 stratification was weaker.

451 The interior of the filament exhibited modest levels of chlorophyll-a fluo-  
452 rescence relative to the filament edges. In particular at the furthest offshore  
453 extent of the survey, fluorescence was at its lowest values of  $\leq 0.1 \text{ V}$  within a  
454 narrow band of 20 km horizontal extent coinciding with the cool, fresh wa-  
455 ter of the filament. Where the isopycnals outcropped, fluorescence  $\geq 0.7 \text{ V}$ .  
456 Closer inshore, fluorescence exceeded  $0.8 \text{ V}$  at the southern ends of legs 4 and  
457 5 where strong gradients in temperature and salinity occurred but for which  
458 there was no corresponding lateral density front. Chlorophyll concentrations  
459 were thus highest towards the periphery of the filament rather than within  
460 its core.

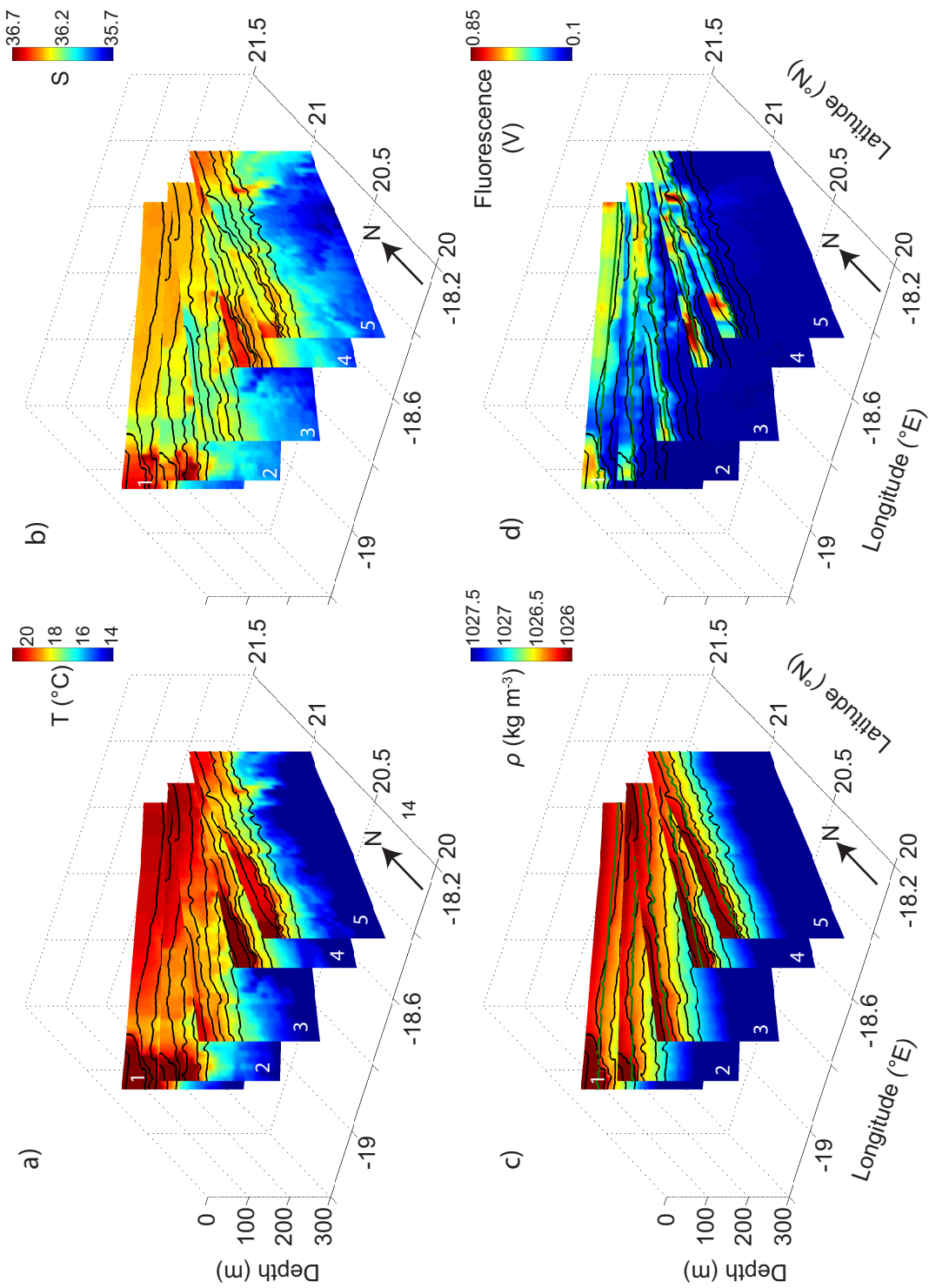


Figure 6: a) Temperature, b) salinity, c) density, and d) fluorescence measured during MVP1, the survey of the primary filament within which Patch 1 was completed. The legs are numbered in accordance with Fig. 2. Isopycnals within the range of  $1026 \leq \rho \leq 1027 \text{ kg m}^{-3}$  are overlain on each panel every  $0.02 \text{ Kg m}^{-3}$ . North is indicated by the back arrow.

461 *3.3. Susceptibility to frontal instabilities*

462 To assess the susceptibility of the filament environment to submesoscale  
463 instabilities as a mechanism supplying nutrients in the absence of sufficient  
464 vertical turbulent entrainment or Ekman pumping, the hydrographic data  
465 obtained from the MVP was combined with the VM-ADCP data to provide  
466 information on the filament dynamical regime. In particular, as the Rossby  
467 number,  $Ro$ , approaches unity the flow is likely to become unstable and de-  
468 velop secondary ageostrophic motions. At the spatial scales of the filament  
469 front, in-situ measurements of both velocity components,  $U$  and  $V$ , are re-  
470 quired to compute their horizontal gradients. Given the inability of a single  
471 ship to neither measure gradients in both eastward and northward directions  
472 simultaneously, nor separately over a short enough time scale to eliminate  
473 the possibility of the flow evolving, we approximate the local relative vorticity,  
474  $\zeta = \frac{\partial v}{\partial x} - \frac{\partial u}{\partial y}$  using one velocity component only in the usual manner  
475 for such studies. Due to the dominance of the frontal flow and the design  
476 of the surveys to cross the filament perpendicular to the front orientation  
477 on each transect, VM-ADCP velocities were rotated to cross-front (flow ori-  
478 entated perpendicular to the front) and along-front (parallel to the front)  
479 components. The along-front velocity component was much larger than the  
480 cross-front component due to the dominance of the geostrophic flow, in par-  
481 ticular at the southern end of legs 2 and 3 where the outcropping isopycnals  
482 were most pronounced (Fig. 7). Most notably, currents were directed offshore  
483 within the middle of the filament (approximately 30-60 km) before rotating  
484 to an inshore direction at the southern extent of each leg as the density front  
485 was crossed on the filament edge. During leg 2, along-front velocity exceeded  
486  $0.4 \text{ m s}^{-1}$ , more than twice the maximum velocities directed normal to the  
487 front.

488 Largest  $U_{along}$  (i.e. along-front flows) was observed on the southern edge of  
489 the filament where currents of  $\sim 0.25 \text{ m s}^{-1}$  were directed primarily eastward,  
490 i.e. towards the coast (Fig. 8a). In contrast, offshore flow dominated currents  
491 within the filament and attained westward magnitudes larger than than the  
492 eastward frontal geostrophic flow in the south. Despite the absence of an  
493 equivalently strong frontal signature at the northern edge of the filament, it is  
494 likely that the weaker (compared to the eastward flow in the south) westward  
495 frontal flow reinforced the offshore flow within the filament. As a result of  
496 the superposition of the frontal flow on the mean offshore advection, there is  
497 thus no distinct dynamic signature associated with the northern front.

498 The strong vorticity associated with the frontal jets on the southern edge

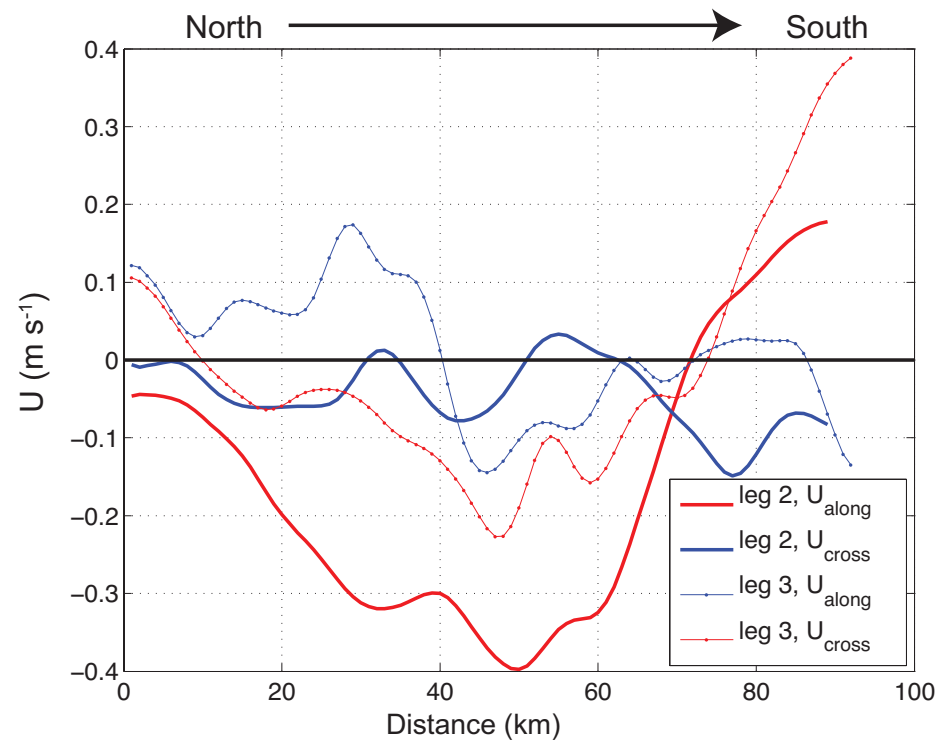


Figure 7: Along (red) and cross-front (blue) velocities during legs 2 (solid line) and 3 (dotted line). The along-front velocity component is estimated as the current directed perpendicular to the ship's direction of travel given the aim of crossing the front at right angles to its local orientation during each leg. Note the distinct increase in positive along-front currents (directed to the south-east during legs 2 and 3) at the southern edge of each leg in accordance with that expected for thermal wind balance at the outcropping isopycnals.

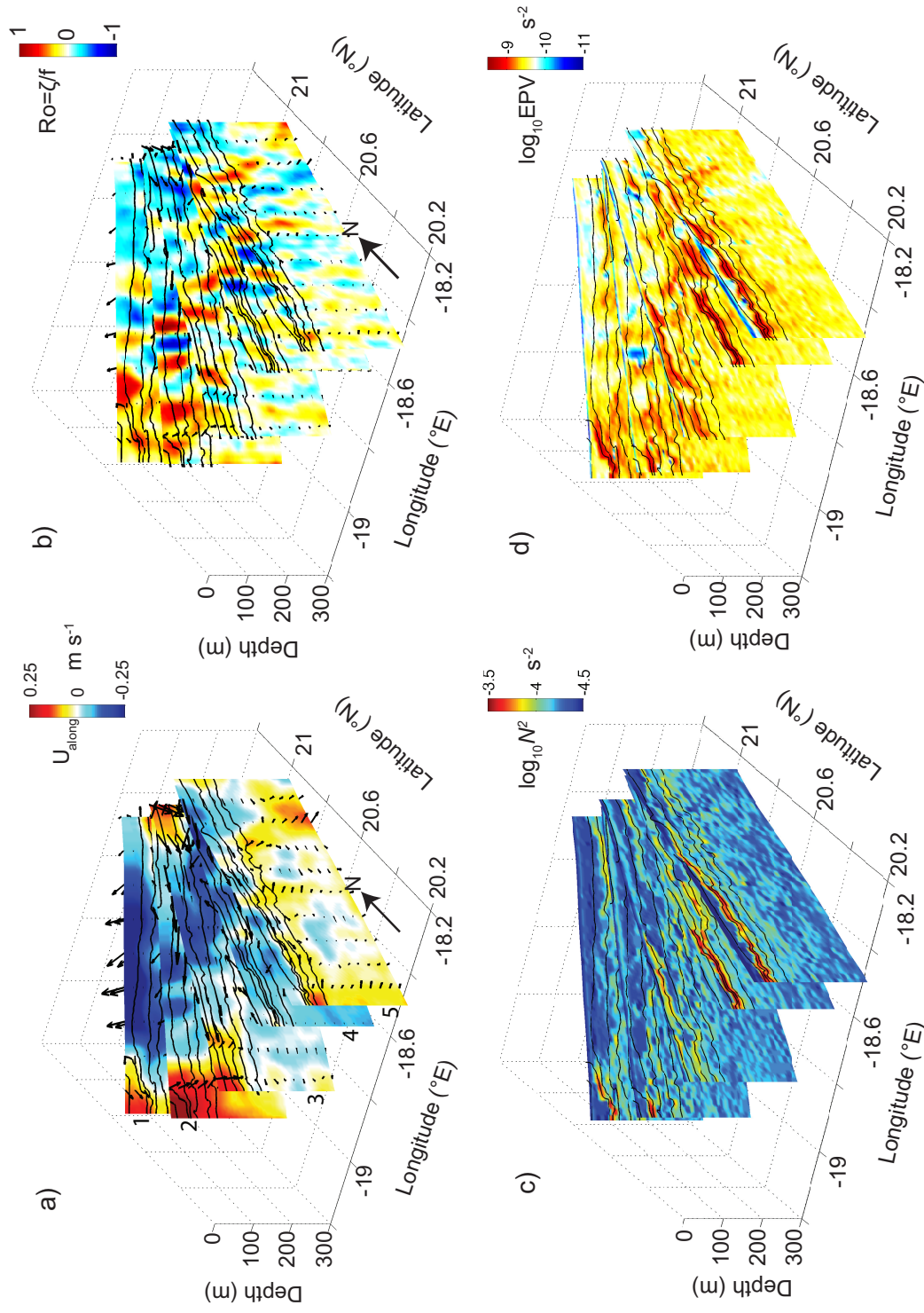


Figure 8: a) Cross-track (along-front) velocity component, b) Rossby number  $\zeta/f$ , c)  $N^2$ , and d) EPV during filament survey. The Ertel Potential Vorticity (EPV) is estimated by Eq. 6 by approximating the relative vorticity as the along-track gradient in the cross-track velocity. This approximation is more accurate in frontal regions where the flow is dominated by along-front geostrophic jets generated from the sloping isopycnals (Overlain in a)-d) as in Fig. 6). Velocity vectors are included and illustrate the primary direction and magnitude of flow, in particular at the strongly defined front at the southern edge of legs 1-3.

499 of the filament generated large Rossby numbers (Fig. 8b). Within several  
 500 km of the outcropping isopycnals during legs 1 and 2 in particular,  $Ro$  ap-  
 501 proaches unity within localised regions just inside the front. Values of  $Ro$  are  
 502 largely positive in accordance with the numerical modelling results of Ma-  
 503 hadevan and Tandon (2006). The opposite sense of velocity veering across  
 504 the northern edge of the filament generated weaker, negative  $Ro$  of  $\sim 0.2$ , pos-  
 505 sibly due to the weakened signature of the frontal flow by the mean offshore  
 506 flow within the filament.

507 The extent to which the filament fronts are subject to frontogenesis from  
 508 which submesoscale instabilities can subsequently emerge is quantified by  
 509 the potential vorticity (PV) (Thomas and Lee, 2005), which depends on the  
 510 relative vorticity of the flow, stratification and lateral density gradients. We  
 511 thus consider the transects during MVP1 as cross-front sections for which  
 512  $U_{cross}$ , constitutes the along-front flow in a 2D approximation for PV,  $q_{2d}$ ,

$$q_{2d} = \frac{-gf}{\rho_o} \left[ \left( f - \frac{\partial U}{\partial y} \right) \frac{\partial \sigma_\theta}{\partial z} + \frac{\partial U}{\partial z} \frac{\partial \sigma_\theta}{\partial y} \right] \quad (6)$$

513 Numerical simulations demonstrate that, within regions of negative PV,  
 514 lateral density gradients within the surface mixed layer become symmetri-  
 515 cally unstable, generating slantwise convection within submesoscale fronts  
 516 (Thomas and Taylor, 2010). In our observations, lowest PV is found in the  
 517 weakly stratified SML at the southern edge of leg 5 (Fig. 8c,d). Throughout  
 518 the study region the PV is dominated by the influence of the stratification  
 519 compared to that of relative vorticity or lateral density gradients. The strong  
 520 front at the southern edge of legs 1 and 2 exhibit high PV within the strongly  
 521 stratified sloping isopycnals despite the strong vorticity; the rotation of the  
 522 velocity vectors across the front is in the sense to increase the vorticity term  
 523 in Eq. 6 and thus the PV. In contrast the weaker stratification and oppo-  
 524 site sense of rotation towards the northern front lowers the PV, rendering  
 525 it more susceptible to frontogenetically induced instabilities and symmetric  
 526 instability.

### 527 3.4. Patch 2: Submesoscale circulations and subduction

528 The mesoscale MVP/VM-ADCP survey of the primary filament demon-  
 529 strated that it's edges were characterised by  $O(1)$  Rossby number and there-  
 530 fore susceptible to the development of submesoscale instabilities (Molemaker  
 531 et al., 2005) despite not providing any direct evidence of their role. Imme-  
 532 diately following the large-scale survey and Patch 1, Patch 2 targeted what



533 appeared to be an emerging filament. The drifters were deployed close to  
534 an upwelling front across which temperature increased from 17°C to nearly  
535 19°C in less than 10 km(Fig. 9). The front was also demarcated by high  
536 chlorophyll concentrations on the northern (warm) side of the front, consis-  
537 tent with local upwelling supplying nutrient rich water to the surface and  
538 stimulating new production.

539 An initial survey prior to SF<sub>6</sub> nighttime mapping revealed strong cyclonic  
540 vorticity within the surface layers; currents within the emerging filament were  
541 directed towards the filament edge where they rotated to become aligned with  
542 the front, presumably due to the influence of the along-front jet observed in  
543 the mesoscale filament survey (Fig. 9a). The vorticity signature of the front  
544 was much more pronounced than during MVP1 where the dynamic signature  
545 of the front on the northern edge of the filament was obscured. The strongest  
546 vorticity was observed as the ship passed through the northern front from  
547 the cold water into the warmer, chlorophyll-rich water at 18°W, 21°30'N.  
548 Assuming that the rotation of the velocity at 26 m, which is the shallowest  
549 bin for which good data were available, was dominated by the frontal current  
550 we estimate the 2D vorticity in the similar manner to described above. The  
551 observed velocities are rotated to be along and across-track and the cross-  
552 frontal gradient in along-front velocity used to estimate  $\zeta$ .  $Ro \geq 1$  almost  
553 everywhere along the northern half of the eastern leg in Fig. 9a but reach a  
554 maximum (absolute) value of  $Ro = -6.6$  at the end of the leg where the tracer  
555 was released and the along-front velocities increase by  $\geq 0.1 \text{ m s}^{-1} \text{ km}^{-1}$ .

556 As with Patch 1, a quantity of SF<sub>6</sub> was released following deployment of  
557 the Wirewalker drifter. The tracer was initially constrained within a patch  
558 of approximately  $5 \times 5 \text{ km}$  horizontal extent but 24 hours later had become  
559 elongated in a north-east/south-west direction (Fig. 9d). More significantly,  
560 the SF<sub>6</sub> concentration measured at the ship's intake at 4 m depth over the  
561 same 24 hour period from  $t=128$  to  $t=129$  decreased by an order of magnitude  
562 from  $10^3 \text{ fmol l}^{-1}$  to  $10^2 \text{ fmol l}^{-1}$ (Fig. 9). Water samples taken from a CTD  
563 profile indicated that the SF<sub>6</sub> had been subducted out of the upper 50 m into  
564 the underlying stratification and elongated into a narrow filament. The vor-  
565 ticity signature and vertical current shear,  $\partial U / \partial z \geq 3 \times 10^{-3} \text{ s}^{-1}$ , remained  
566 coherent throughout the upper 100 m. Given the biogeochemical objectives  
567 of the cruise to monitor the primary production within the upwelled water,  
568 the experiment was subsequently terminated.

569 Direct evidence of the rapid vertical velocities implicated in the rapid  
570 subduction of the SF<sub>6</sub> were obtained from the drifting ADCP. Following



571 their release, the Wirewalker and drifting ADCP twice approached the front  
572 depicted in Fig. 9. On each occasion the drifter measured an increase in  
573 temperature (and decrease in density) at the same time as persistent, coher-  
574 ent downward velocities of  $\geq 4 \text{ mm s}^{-1}$ , equating to  $\geq 350 \text{ m day}^{-1}$  (Fig. 10).  
575 The drifters remained within the downwelling current for approximately 1-2  
576 hours before being advected back out of the front into the cooler filament wa-  
577 ter. As the drifters did not completely cross the front, they did not have the  
578 opportunity to measure the upwelling that would be expected as the return  
579 part of the thermally direct overturning circulation associated with the sub-  
580 mesoscale front; numerical simulations demonstrate that downwelling occurs  
581 on the cold side of the front and upwelling on the warm side (Mahadevan and  
582 Tandon, 2006; Thomas and Lee, 2005). The maximum observed downwelling  
583 velocity occurred at  $y=130.95$  as the drifters reached the front as evidenced  
584 by strongly sloping isotherms measured by the Wirewalker. Temperature  
585 increased from  $16.8^\circ\text{C}$  to  $18^\circ\text{C}$  within 2 hours and  $w$  reached  $8 \text{ mm s}^{-1}$  at a  
586 depth of 60 m, i.e. below the surface as suggested by Mahadevan and Tandon  
587 (2006).

## 588 4. Discussion

### 589 4.1. Submesoscale instabilities at the edge of upwelling filaments

590 The edges of mesoscale filaments created in response to coastal upwelling  
591 in an eastern boundary current have been demonstrated in numerical sim-  
592 ulations to be highly susceptible to submesoscale instabilities (Capet et al.,  
593 2008a,b). The mechanism triggering the cascade of energy to smaller scale  
594 motions from an initial geostrophically balanced state is surface-intensified  
595 frontogenesis where surface horizontal density gradients are intensified by a  
596 confluent flow field. Local regions of high Rossby number emerge and per-  
597 mit the development of secondary instabilities that manifest themselves as  
598 intense vertical circulations at fronts, with downwelling on the cold side of  
599 the front and upwelling on the warm side. In our observations, the desta-  
600 bilisation of the front encircling the filament may have been accelerated by  
601 wind stress blowing in the direction of the along-front jet and generating a  
602 nonlinear Ekman transport that would advect cold fluid over the front to  
603 the warm side, triggering convective instabilities and further enhancing the  
604 break down in geostrophic balance. The process is intermittent and spatially  
605 localised. The resulting new production facilitated by the injection of nutri-  
606 ents is known to be episodic at timescales commensurate with the ephemeral

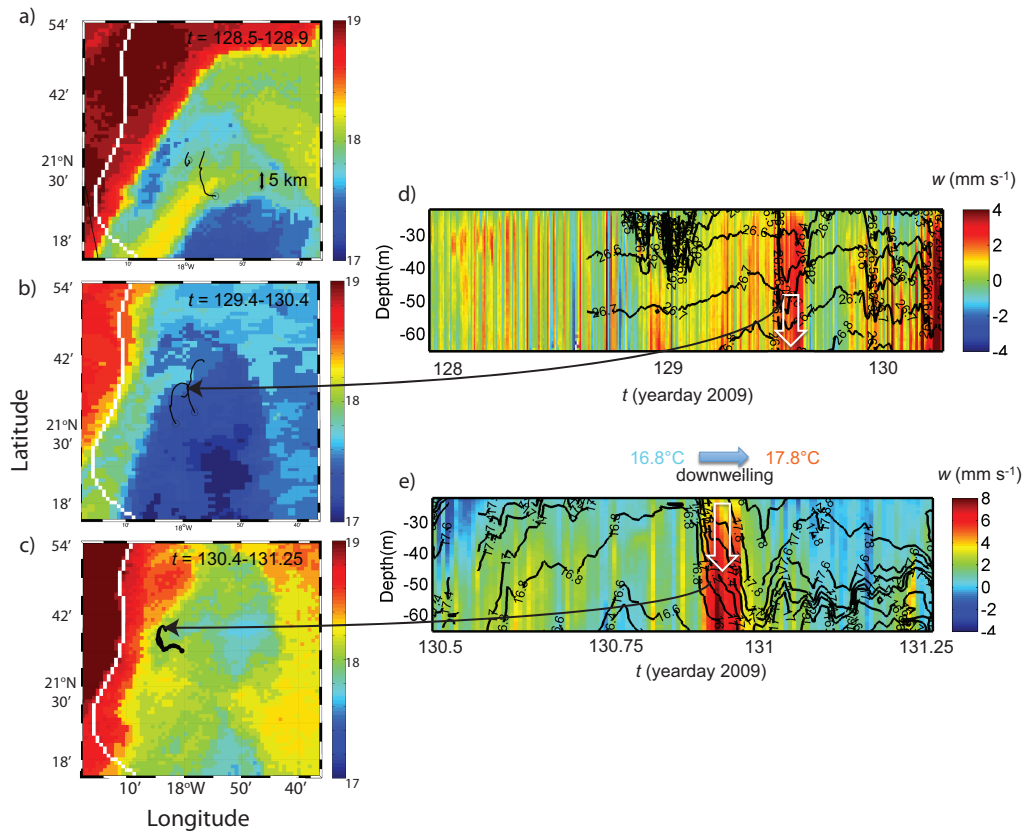


Figure 10: SST during days *a*) 128, *b*) 129 and *c*) 130, and vertical velocities measured by the drifting ADCP over the periods *d*)  $t = 128 - 130.25$  and *e*)  $t = 130.5 - 131.25$ . The intense downwelling at  $t=129.7$  in *d*) and  $130.9$  in *e*) occur at precisely the time that the drifter passed nearest the front observed in the remote sensing images (indicated by the long black arrows between *b*) - *d*) and *c*) - *e*). The drifter track for the period over which the SST data were collected in each image is indicated in *a*) - *c*) by the black line. Black lines in *d*) and *e*) correspond to isopycnals and isotherms, respectively.

607 nature of submesoscales themselves and spatially patchy (Levy et al., 2012).  
608 The patchy production is particularly pronounced in the remote sensing im-  
609 age for chlorophyll-a depicted by Fig. 1.

610 Our observations are entirely consistent with the dynamic environment  
611 elucidated by Capet et al. (2008a,b) and who further suggest that their ef-  
612 fects on biogeochemical exchange may be quite important. They are also in  
613 direct contrast to the findings of Gruber et al. (2011) who propose, on the ba-  
614 sis of an eddy resolving (but not submesoscale-resolving) model and satellite  
615 observations, that within the same upwelling region as we have presented bi-  
616 ological production is actually suppressed. The towed CTD and VM-ADCP  
617 surveys highlighted that the filament periphery was characterised by strong  
618 vorticity associated with the frontal jets and order unity Rossby numbers.  
619 The mesoscale environment is thus susceptible to frontogenesis and the de-  
620 velopment of submesoscale instabilities that are demonstrated by numerical  
621 simulations to be intermittent in time and space, and to manifest themselves  
622 as intense vertical velocities in narrow filaments of strong cyclonic vorticity  
623 (Mahadevan and Tandon, 2006). The vertical velocities measured by the  
624 drifting ADCP as it approached a temperature front during Patch 2, and the  
625 rapid subduction of tracer, provide direct evidence of submesoscale vertical  
626 circulations in teh observations presented here. Accompanied by pronounced  
627 cyclonic vorticity for which there has been demonstrated a strong preponder-  
628 ance in simulations (e.g. Levy et al. (2001); Mahadevan and Tandon (2006)),  
629 the encountering of an intense downwelling flow on the cold side of the front  
630 indicates that there is almost certainly an accompanying upwelling on the  
631 warm side of the front. We did not observe the upwelling, however, because  
632 the drifters did not cross front to the warm side.

633 Two outstanding issue remain; firstly, where the additional nutrients were  
634 fed into the system and secondly, how did the nutrients upwelled on the warm  
635 side of the front cross to the inside of the filament where they were able to  
636 stimulate new production? With respect to the location of the instabilities  
637 and resupply of nutrients, the new production was observed to be higher  
638 than expected at the position where the front changed its orientation from  
639 meridional to zonal. The importance of the orientation lies in the effective-  
640 ness of the wind stress to generate a cross-front Ekman buoyancy flux by  
641 blowing down front. Through so doing, the wind stress interacts with the  
642 low frequency vorticity of the frontal jet to advect dense surface water across  
643 the front, thereby triggering convective instabilities that intensify the frontal  
644 circulations. The anatomy of the filament would indicate that the persistent

645 northerly wind stress in the Cap Blanc region was (and always will be given  
646 the ubiquity of the wind direction) aligned with the frontal jet in two pri-  
647 mary locations; firstly, along the initial upwelling front that runs parallel to  
648 the coast and to the east of which in our observations the SF<sub>6</sub> was released.  
649 Secondly, a southward flowing jet was observed in Fig. 8 on the southern  
650 side of the filament at its furthest offshore extent and was laterally localized  
651 to the extent that the relative vorticity associated with the its horizontal,  
652 cross-front gradient, generated  $O(1)$  Rossby number.

653 Despite the apparent inconsistency in the location at which the new pro-  
654 duction was enhanced and the frontal orientation that was largely perpen-  
655 dicular to the wind stress where excessive production was observed, we note  
656 that the nutrients upwelled along the filament periphery will be advected  
657 by the frontal jet, thereby becoming available to stimulate new production  
658 downstream of the injection location. There is thus a remote effect of the  
659 upwelling on new production when considered in an along-front sense. Sec-  
660 ondly, new production will be stimulated nearer the front where the upwelled  
661 nutrients are concentrated. During the first half of Patch 1, the drifters and  
662 thus centre of the Lagrangian reference frame were located more than 30 km  
663 from the front and would not have been able to access the nutrients made  
664 available near the front by submesoscale instabilities. It was not until the  
665 drifters became entrained in the frontal flow on day 115 that our observa-  
666 tions were made within a nutrient enriched region. The remote effect of  
667 submesoscales on new production has been discussed by Lévy et al. (2012)  
668 but refers to much longer timescales of variability that are more consistent  
669 with the oceanic gyres than with the short spatiotemporal scales discussed  
670 here. We have focussed on Patches 1 and 2 in this paper because the avail-  
671 able data permit a degree of confidence in the interpretation of the results;  
672 during Patch 3 no MVP data were acquired and so we are not able to assess  
673 the susceptibility of the filament edges to submesoscale instabilities. How-  
674 ever, Fig. 11 demonstrates that the mismatch within the southern filament  
675 was very small, implying that there was no influence of additional nutrients  
676 on new production. In contrast to Patch 1, however, the Lagrangian refer-  
677 ence frame in which the measurements were made was always far from the  
678 front. Secondly, the front was considerably weaker than the primary filament  
679 discussed earlier when viewed in terms of the magnitude of SST gradients.

680 The mechanism by which nutrients upwelled on the warm side of the  
681 filament edge encroach into the filament is less clear. Satellite images of an  
682 upwelling filament within the Californian eastern boundary current system

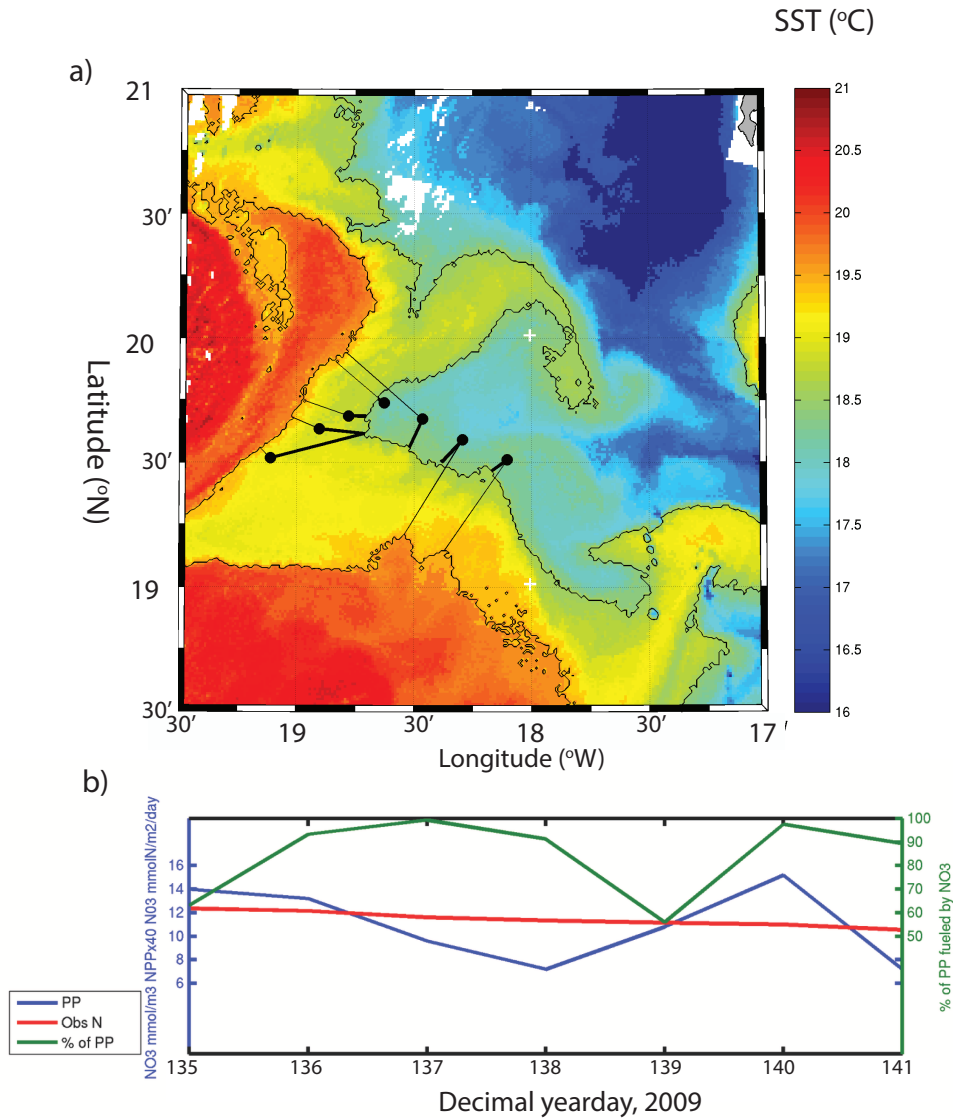


Figure 11: Summary of conditions during Patch 3, which was conducted further south and approximately 3 weeks after Patch 1. a) SST ( $^{\circ}\text{C}$ ) throughout study region of Patch 3 during day 137 and the position of the drogued drifter (black) relative to the nearest location of front at the filament periphery (black line, defined as  $18.5^{\circ}\text{C}$  isotherm); b) nitrate concentration (red line), new production (blue line) and the percentage of the new production that can be explained by the observed nitrate concentration (green line) throughout Patch 3.

683 provide clear evidence of warm water filaments intruding into the main body  
684 of the filament (Figure 16 in Capet et al. (2008b)). As submesoscales are  
685 ephemeral and short-lived, the filaments decay and, in the case of nutrient-  
686 rich filaments generated on the warm side of the front, diffuse the tracers that  
687 they contain into the surrounding water. Under such a scenario, the nutrients  
688 that we propose are brought to the surface by the intense circulations at  
689 the filament periphery would be made available within the colder upwelled  
690 water inside the front. Additional work is required in this area to evaluate  
691 the behavior and fate of the nutrients within a rapidly evolving dynamic  
692 system; Levy et al. (2012) discuss how the timescales of variability associated  
693 with submesoscale circulations may actually render them quite ineffective in  
694 stimulating new production as compared to mesoscales for which the supply  
695 of nutrients is lower but more persistent over biologically relevant timescales.

## 696 5. Conclusions

697 Observations made during a cruise to the eastern boundary current up-  
698 welling system off Cap Blanc indicate that nutrients upwelled to the euphotic  
699 zone inshore of the coastal front stimulate high levels of primary production.  
700 The coastal front develops mesoscale instabilities and forms filaments of up-  
701 welled water that extend several hundreds of kilometers offshore. As the  
702 nutrient-rich water was advected offshore within the filament, new produc-  
703 tion remained higher than can be explained by the locally available nutrients  
704 and vertical fluxes across the base of the euphotic layer. Specifically, only  
705 60% of the new production could be explained by the local nutrient and ver-  
706 tical fluxes, implying that additional nutrients were being supplied to the  
707 interior of the filament.

708 A large-scale towed CTD and vessel-mounted ADCP survey of the fil-  
709 ament within which the mismatch was observed indicate that the periph-  
710 eral edges of the filament were characterized by strong relative vorticity and  
711 Rossby numbers approaching unity, rendering the frontal environment sus-  
712 ceptible to the generation of submesoscale instabilities. The southern edge  
713 of the filament in particular was demarcated by a strong lateral buoyancy  
714 gradient and distinct frontal jet that flowed parallel to the outcropping isopy-  
715 cnals. Chlorophyll-a concentrations were patchy but intensified at the fila-  
716 ment edges, consistent with the local injection of nutrients to the euphotic  
717 zone where lateral buoyancy gradients and vorticity were elevated.



718 Direct evidence for the role played by submesoscales circulations was  
719 found during the second Lagrangian Patch experiment that aimed to study  
720 the draw-down of nutrients within a newly-forming filament of upwelled wa-  
721 ter. The SF<sub>6</sub> tracer was injected at the surface immediately adjacent to  
722 a strong temperature front across which the horizontal velocity rotated cy-  
723 clonically, generating negative Rossby numbers with an absolute magnitude  
724 of  $\geq 5$  when local relative vorticity,  $\zeta$ , was approximated as the along-track  
725 gradient in cross-front velocity. Within 24 hours the tracer concentration  
726 had decreased by an order of magnitude due to its subduction out of the sur-  
727 face layers and become constrained within an elongated patch that aligned  
728 with the front. Over the two days for which the drifters were deployed,  
729 downwelling vertical velocities  $\geq 350$  m day<sup>-1</sup> were observed on three sepa-  
730 rate occasions at the precise moment that they approached the front from  
731 the cold side. Thus the vertical velocities and tracer behaviour displayed the  
732 properties of thermally direct overturning circulations predicted by numerical  
733 simulations to occur within elongated filaments of negative vorticity.

734 It remains unclear where the nutrients are resupplied to the filament given  
735 the localized regions within which wind stress is aligned with the frontal cur-  
736 rents. Whilst not the only mechanism capable of generating submesoscale  
737 instabilities within frontal regions, it remains the most likely explanation for  
738 the injection of nutrients that we observed. The effects on biological produc-  
739 tion are not localized to the sites of active submesoscale upwelling but may  
740 be remote due to the advection of nutrients down front by the geostrophic jet.  
741 Similarly, there is some evidence that the nutrients upwelled on the warm  
742 side make themselves available for new production within the mesoscale fil-  
743 ament by becoming entrained in submesoscale filaments that intrude into  
744 the cold upwelled water. As the submesoscale features are ephemeral and  
745 comparatively short-lived, the nutrients that they contain thereafter become  
746 available within the main filament following their decay.

## 747 **Acknowledgements**

748 This work was funded by UK NERC grant NE/C517176/2. The authors  
749 thank the NERC Earth Observation Data Acquisition and Analysis Service  
750 (NEODAAS) for supplying data in this study. We thank the National Marine  
751 Facilities staff for their assistance in operating the MVP and the captain and  
752 crew of the RRS *Discovery* for their help throughout the D338 cruise. Torres

753 was additionally supported by the NERC National Capability in Modelling  
754 programme at the Plymouth Marine Laboratory.

## 755 **References**

756 Barnes, S.L., 1994. Applications of the Barnes Objective Analysis Scheme.  
757 Part I: Effects of Undersampling, Wave Position, and Station Random-  
758 ness. *Journal of Atmospheric and Oceanic Technology* 11, 1433–1448.  
759 doi:10.1175/1520-0426.

760 Blackburn, T.H., 1979. Method for measuring rates of  $\text{NH}_4^+$  turnover in  
761 anoxic marine sediments, using a  $^{15}\text{N}$ - $\text{NH}_4^+$  dilution technique. *Applied*  
762 *and Environmental Microbiology* 37, 760–765.

763 Caperon, J., Schell, D., Hirota, J., Laws, E., 1979. Ammonium excretion  
764 rates in Kaneohe Bay, Hawaii, measured by a  $^{15}\text{N}$  isotope dilution tech-  
765 nique. *Marine Biology* 54, 33–40.

766 Capet, X., McWilliams, J.C., Molemaker, M.J., Shchepetkin, A.F., 2008a.  
767 Mesoscale to Submesoscale Transition in the California Current System.  
768 Part I: Flow Structure, Eddy Flux, and Observational Tests. *Journal of*  
769 *Physical Oceanography* 38, 29–43. doi:10.1175/2007JPO3671.1.

770 Capet, X., McWilliams, J.C., Molemaker, M.J., Shchepetkin, A.F., 2008b.  
771 Mesoscale to Submesoscale Transition in the California Current System.  
772 Part II: Frontal Processes. *Journal of Physical Oceanography* 38, 44–64.  
773 doi:10.1175/2007JPO3672.1.

774 Clark, D.R., Fileman, T.W., Joint, I., 2006. Determination of am-  
775 monium regeneration rates in the oligotrophic ocean by gas chro-  
776 matography/mass spectrometry. *Marine Chemistry* 98, 121–130.  
777 doi:10.1016/j.marchem.2005.08.006.

778 Clark, D.R., Miller, P.I., Malcolm, E., Woodward, S., Rees, A.P., 2011.  
779 Inorganic nitrogen assimilation and regeneration in the coastal upwelling  
780 region of the Iberian Peninsula. *Limnology and Oceanography* 56, 1689–  
781 1702. doi:10.4319/lo.2011.56.5.1689.

782 Clark, D.R., Rees, A.P., Joint, I., 2007. A method for the deter-  
783 mination of nitrification rates in oligotrophic marine seawater by gas

- 784 chromatography/mass spectrometry. *Marine Chemistry* 103, 84–96.  
785 doi:10.1016/j.marchem.2006.06.005.
- 786 Clark, D.R., Widdicombe, C.E., Rees, A.P., Malcolm, E., Woodward, S.,  
787 2016. The significance of nitrogen regeneration for new production within  
788 a filament of the Mauritanian upwelling system. *Biogeosciences* 13, 2873–  
789 2888. doi:10.5194/bg-13-2873-2016.
- 790 Fernández, C., Farías, L., Alcaman, M., 2009. Primary produc-  
791 tion and nitrogen regeneration processes in surface waters of the Pe-  
792 ruvian upwelling system. *Progress in Oceanography* 83, 159–168.  
793 doi:10.1016/j.pocean.2009.07.010.
- 794 Fernández I., C., Raimbault, P., 2007. Nitrogen regeneration in the  
795 NE Atlantic Ocean and its impact on seasonal new, regenerated  
796 and export production. *Marine Ecology Progress Series* 337, 79–92.  
797 doi:10.3354/meps337079.
- 798 Gruber, N., Lachkar, Z., Frenzel, H., Marchesiello, P., Münnich, M.,  
799 McWilliams, J.C., Nagai, T., Plattner, G.K., 2011. Eddy-induced re-  
800 duction of biological production in eastern boundary upwelling systems.  
801 *Nature Geoscience* 4, 787–792. doi:10.1038/ngeo1273.
- 802 Huntsman, S.A., Barber, R.T., 1977. Primary production off northwest  
803 Africa: the relationship to wind and nutrient conditions. *Deep Sea Re-*  
804 *search* 24, 25–33. doi:10.1016/0146-6291(77)90538-0.
- 805 Ikeda, M., Emery, W.J., 1984. Satellite observations and modeling of mean-  
806 ders in the California Current System off Oregon and northern California.  
807 *Journal of Physical Oceanography* 14, 1434–1450.
- 808 Lathuiliere, C., Levy, M., Echevin, V., 2010. Impact of eddy-  
809 driven vertical fluxes on phytoplankton abundance in the eu-  
810 photic layer. *Journal of Plankton Research* 33, 827–831. URL:  
811 <http://www.plankt.oxfordjournals.org/cgi/doi/10.1093/plankt/fbq131>,  
812 doi:10.1093/plankt/fbq131.
- 813 Levy, M., Ferrari, R., Franks, P.J.S., Martin, A.P., Rivière, P., 2012. Bringing  
814 physics to life at the submesoscale. *Geophysical Research Letters* 39, 1–13.  
815 doi:10.1029/2012GL052756.

- 816 Lévy, M., Iovino, D., Resplandy, L., Klein, P., Madec, G., Tréguier, A.M.,  
817 Masson, S., Takahashi, K., 2012. Large-scale impacts of submesoscale  
818 dynamics on phytoplankton: Local and remote effects. *Ocean Modelling*  
819 43-44, 77–93. doi:10.1016/j.ocemod.2011.12.003.
- 820 Levy, M., Klein, P., Treguier, A.M., 2001. Impact of sub-mesoscale physics  
821 on production and subduction of phytoplankton in an oligotrophic regime.  
822 *Journal of Marine Research* 59, 535–565.
- 823 Li, Q.P., Dong, Y., Wang, Y., 2016. Phytoplankton dynamics driven by ver-  
824 tical nutrient fluxes during the spring inter-monsoon period in the north-  
825 eastern South China Sea. *Biogeosciences* 13, 455–466. doi:10.5194/bg-13-  
826 455-2016.
- 827 Loucaides, S., Tyrrell, T., Achterberg, E.P., Torres, R., Nightingale, P.D.,  
828 Kitidis, V., Serret, P., Woodward, M., Robinson, C., 2012. Biological  
829 and physical forcing of carbonate chemistry in an upwelling filament off  
830 northwest Africa: Results from a Lagrangian study. *Global Biogeochemical*  
831 *Cycles* 26. doi:10.1029/2011GB004216.
- 832 Mahadevan, A., D’Asaro, E., Lee, C., Perry, M.J., 2012. Eddy-driven strat-  
833 ification initiates North Atlantic spring phytoplankton blooms. *Science*  
834 337, 54–8. doi:10.1126/science.1218740.
- 835 Mahadevan, A., Tandon, A., 2006. An analysis of mechanisms for subme-  
836 soscale vertical motion at ocean fronts. *Ocean Modelling* 14, 241–256.  
837 doi:10.1016/j.ocemod.2006.05.006.
- 838 Martínez-Marrero, A., Rodríguez-Santana, A., Hernández-Guerra, A., Fraile-  
839 Nuez, E., López-Laatzén, F., Vélez-Belchí, P., Parrilla, G., 2008. Distri-  
840 bution of water masses and diapycnal mixing in the Cape Verde Frontal  
841 Zone. *Geophysical Research Letters* 35. doi:10.1029/2008GL033229.
- 842 McGillicuddy, D.J., Anderson, L.a., Bates, N.R., Bibby, T., Buesseler, K.O.,  
843 Carlson, C.a., Davis, C.S., Ewart, C., Falkowski, P.G., Goldthwait, S.a.,  
844 Hansell, D.a., Jenkins, W.J., Johnson, R., Kosnyrev, V.K., Ledwell, J.R.,  
845 Li, Q.P., Siegel, D.a., Steinberg, D.K., 2007. Eddy/wind interactions stim-  
846 ulate extraordinary mid-ocean plankton blooms. *Science (New York, N.Y.)*  
847 316, 1021–6. doi:10.1126/science.1136256.

- 848 Menden-Deuer, S., Lessard, E.J., 2000. Carbon to volume relationships  
849 for dinoflagellates, diatoms, and other protist plankton. *Limnology and*  
850 *Oceanography* 45, 569–579. doi:10.4319/lo.2000.45.3.0569.
- 851 Meunier, T., Barton, E.D., Barreiro, B., Torres, R., 2012. Upwelling filaments  
852 off Cap Blanc: Interaction of the NW African upwelling current and the  
853 Cape Verde frontal zone eddy field? *Journal of Geophysical Research* 117,  
854 C08031. doi:10.1029/2012JC007905.
- 855 Molemaker, M.J., McWilliams, J.C., Yavneh, I., 2005. Baroclinic Instability  
856 and Loss of Balance. *Journal of Physical Oceanography* 35, 1505–1517.  
857 doi:10.1175/JPO2770.1.
- 858 Narimousa, S., Maxworthy, T., 1989. Application of a laboratory  
859 model to the interpretation of satellite and field observations of  
860 coastal upwelling. *Dynamics of Atmospheres and Oceans* 13, 1–46.  
861 doi:http://dx.doi.org/10.1016/0377-0265(89)90032-8.
- 862 Nightingale, P.D., Malin, G., Law, C., Watson, A.J., Liss, P.S., Lid-  
863 dicoat, M.I., Boutin, J., Upstill-Goddard, R.C., 2000. In situ eval-  
864 uation of air-sea gas exchange parameterizations using novel conserva-  
865 tive and volatile tracers. *Global Biogeochemical Cycles* 14, 373–387.  
866 doi:10.1029/1999GB900091.
- 867 Olenina, I., Hajdu, S., Edler, L., Andersson, A., Wasmund, N., Busch, S.,  
868 Gobel, J., Gromisz, S., Huseby, S., Huttunen, M., Jaanus, A., Kokko-  
869 nen, P., Ledaine, I., E. Niemkiewicz, 2006. Biovolumes and size-classes of  
870 phytoplankton in the Baltic Sea, in: *Baltic Sea Environment Proceedings*.
- 871 Osborn, T.R., 1980. Estimates of the Local Rate of Vertical Diffusion from  
872 Dissipation Measurements. *Journal of Physical Oceanography* 10, 83–89.
- 873 Owens, N.J.P., Rees, A.P., 1989. Determination of Nitrogen<sup>45</sup> at Sub-  
874 microgram Levels of Nitrogen Using Automated Continuous-flow Isotope  
875 Ratio Mass Spectrometry. *Analyst* 114, 1655–1657.
- 876 Perez-Rodriguez, P., Pelegrí, J.L., Marrero-Diaz, A., 2001. Dynamical char-  
877 acteristics of the Cape Verde frontal zone. *Scientia Marina* 65, 241–250.
- 878 Pinkel, R., Goldin, M.A., Smith, J.A., Sun, O.M., Aja, A.A., Bui, M.N.,  
879 Hughen, T., 2010. The Wirewalker: A Vertically Profiling Instrument

- 880 Carrier Powered by Ocean Waves. *Journal of Atmospheric and Oceanic*  
881 *Technology* 28, 426–435. doi:10.1175/2010JTECHO805.1.
- 882 Thomas, L.N., Lee, C.M., 2005. Intensification of Ocean Fronts by  
883 Down-Front Winds. *Journal of Physical Oceanography* 35, 1086–1102.  
884 doi:10.1175/JPO2737.1.
- 885 Thomas, L.N., Tandon, A., Mahadevan, A., 2008. Submesoscale processes  
886 and dynamics, in: Hecht, M.W., Hasumi, H. (Eds.), *Ocean Modeling in an*  
887 *Eddying Regime*, Geophysical Monograph Series, Volume 177. American  
888 Geophysical Union, Washington DC, pp. 17–38.
- 889 Thomas, L.N., Taylor, J.R., 2010. Reduction of the usable wind-work on the  
890 general circulation by forced symmetric instability. *Geophysical Research*  
891 *Letters* 37, 1–5. doi:10.1029/2010GL044680.
- 892 Woodward, E., Rees, A., 2001. Nutrient distributions in an anticyclonic eddy  
893 in the northeast Atlantic Ocean, with reference to nanomolar ammonium  
894 concentrations. *Deep Sea Research Part II: Topical Studies in Oceanogra-*  
895 *phy* 48, 775–793. doi:10.1016/S0967-0645(00)00097-7.
- 896 Yool, A., Martin, A.P., Fernández, C., Clark, D.R., 2007. The signifi-  
897 cance of nitrification for oceanic new production. *Nature* 447, 999–1002.  
898 doi:10.1038/nature05885.